TAMPEREEN TEKNILLINEN YLIOPISTO
TAMPERE UNIVERSITY OF TECHNOLOGY

LIISA-IDA SORSA

REALISTIC ASTEROID INTERIOR MODELS AND FULL-WAVE TOMOGRAPHY SIMULATION

Master of Science thesis

Examiner: Asst. Prof. Sampsa Pursiainen
Examiner and topic approved by the
Dean of the Faculty of Science and Engineering on 8 August 2018

ABSTRACT

LIISA-IDA SORSA: Realistic asteroid interior models and full-wave tomography simulation
Tampere University of Technology
Master of Science thesis, 47 pages, 0 Appendix pages
August 2018
Master's Degree Programme in Science and Engineering
Major: Mathematics
Examiner: Asst. Prof. Sampsa Pursiainen
Keywords: radar tomography, asteroid, realistic model, radar, inverse problem

The aim of this thesis is to develop a realistic deep interior model for a rubble-pile asteroid and conduct full-wave computed radar tomography on the developed model. The surface model of the asteroid Itokawa is used to develop a finite element mesh including a surface layer of loose soil and regolith coupled with a Gaussian random field which models the realistic interior of a small solar system body. Further structural details such as a void, very loose material space, various cracks and a boulder are added to the realistic interior to investigate the detection power of a bistatic computed radar tomography system.

The results show that a bistatic radar system detects deep interior voids, cracks and boulders in a realistic asteroid. The simulation results and reconstructions show similar radargram profiles as actual radar measurements. The shape and size of voids, loose material, boulders and shallow cracks can be discerned. The deep crack is detectable, but lacks detail. Based on the results of this work, radar tomography is a very promising technique to explore the deep interior of small solar system bodies.

TIIVISTELMÄ

Tampereen teknillinen yliopisto
Diplomityö, 47 sivua, 0 liitesivua
Elokuu 2018
Teknis-luonnontieteellinen koulutusohjelma
Pääaine: Matematiikka
Tarkastajat: Asst. Prof. Sampsa Pursiainen
Avainsanat: tutkatomografia, asteroidi, realistinen malli,tutka, inversio-ongelma

Tämän työn tavoitteena oli kehittää realistinen malli lohkarekasa-asteroidin sisärakenteista ja tutkia mallia tutkatomografiasimulaatioiden avulla. Asteroidi Itokawan pintarakennekuvien peusteella rakennettiin elementtimenetelmäverkko, joka sisälsi asteroidin pintakerroksen lisäksi realistisia asteroidin sisärakenteita kuten tyhjiöonkalo, hyvin huokoinen materiaalirakenne, halkeamia ja tiiviitä lohkareita. Tarkoituksena oli tutkia bistaattisen tutkatomografian kykyä havaita näitä rakenteita realistisen kokoisessa ja rakenteisessa kappaleessa.

Tulokset osoittavat, että bistaattinen tutkatomografiasatelliittisysteemi pystyy havaitsemaan asteroidin syvällä sisärakenteissa olevat onkalot, jotka voivat olla tyhjiöitä, hyvin huokoista materiaalia tai tiiviitä lohkareita. Tutkalla pystyttiin havaitsemaan myös pintakerroksen alapuolinen halkeama hyvin tarkasti. Syvällä asteroidin sisällä oleva halkeama tuotti vain pienen kaiun ja sellaisen tarkka havaitseminen on epävarmaa. Tämän työn perusteella tutkatomografia on erittäin lupaava menetelmä asteroidin sisärakenteiden selvittämisessä.

CONTENTS

LIST OF FIGURES

LIST OF TABLES

LIST OF ABBREVIATIONS AND SYMBOLS

3D three-dimensional

CONCERT Comet Nucleus Sounding Experiment by Radiowave Transmission

ESA European Space Agency

DISCUS Deep Interior Scanning CUbeSat concept

GPR Ground Penetrating Radar

GPU Graphics Processing Unit

JAXA Japanese Aerospace Exploration Agency

NASA National Aeronautics and Space Administration

TCSC Tampere Center for Scientific Computing

α regularization parameter

$\mathbf{A}$ positive semi-definite matrix

A_r aperture of the receiving antenna

β bistatic angle or regularization parameter

B bandwidth

$\vec{B}$ magnetic flux density vector

c speed of light

$\mathbf{\Gamma}$ Tikhonov regularization matrix

δ_r range resolution

$\vec{D}$ electric displacement vector

$\mathbf{D}$ regularization matrix

ε electrical permittivity

ε_0 electrical permittivity of vacuum

ε_r relative electrical permittivity, real-valued

$\vec{E}$ electric field strength vector

f function notation

F function notation

F pattern propagation factor

$\vec{g}$ change in electrical potential

G_t transmitter gain

$\vec{H}$ magnetic field intensity

H^1 Banach space, includes square integrable functions

$\mathbf{I}$ identity matrix

$\vec{J}$ electric current density vector

$\mathbf{L}$ Jacobian matrix resulting from linearization

L_2 functional space for square integrable functions

μ magnetic permeability

$\boldsymbol{\mu}$ expectation of the general multivariate normal distribution

∇ nabla, gradient

$\mathbf{n}$ noise term

Ω computational domain

$\vec{p}$ spatial point at which signal is transmitted

$\mathbf{p}$ vector including points at which signal is transmitted

P_r power at the receiving antenna of a radar

P_t transmitting power

q Electric charge density

r satellite orbiting distance

R_r distance from target to receiver

R_t distance from transmitter to target

R_z rotation matrix around the z axis

σ conductivity distribution (real-valued), or radar cross section

$\boldsymbol{\sigma}^2$ variance

$\boldsymbol{\Sigma}$ covariance matrix

θ angle between satellite and orbiting plane normal

t time, point in time

T time, the end of a time span

$\mathbf{U}$ random variable vector

φ angle covered by orbiting satellite due to its motion

χ_e electrical susceptibility

u electrical potential

$\vec{v}$ test function

w_1 angular frequency of asteroid spin

w_2 angular frequency of a satellite

$\vec{w}$ test fuction

$\vec{x}$ point at which signal is received

$\mathbf{x}$ coordinate vector for permittivity values

$\mathbf{X}$ random variable vector

$\mathbf{y}$ simulated data vector

$\mathbf{y}_{bg}$ simulated background data vector

1. INTRODUCTION

There is water on Mars, reported news agencies around the world on 25 July 2018 [3, 7, 8, 10]. The results of the extensive analysis of the first low-frequency ground penetrating radar ever to orbit another planet [43] spread around the world as soon as they were published. European Space Agency's (ESA) mission Mars Express and its Mars Advanced Radar for Subsurface and Ionospheric Sounding instrument (MARSIS) had sounded the area near the south pole of the planet between May 2012 and December 2015. An anomalously bright subsurface reflections detected by the radar led the group to interpret the feature as a stable body of liquid water on Mars.

Using ground penetrating radar is a well-established geophysical technique to explore the terrestial underground [13]. While the traditional terrestial use of ground penetrating radar involves placing the antenna close to the ground for the detection and imagining of subsurface targets such as underground utilities, pipes, chemical spills, groundwater levels [13], airborne ground penetrating radar was developed to perform cost-effective surveying of the underground in applications which entail the necessity to work with an antenna not in contact with the surveyed structure [22, 23, 51]. Such stepped-frequency continuous wave airborne ground penetrating radar system have been validated to be consistent with results in numerical experiments and measured airborne data [30].

The Apollo 17 mission used a three-wavelength synthetic-aperture radar to probe the subsurface geologic structures of the Moon in 1972 [44]. In other applications in the field of aerospace research, the use of a stepped-frequency Planetary Into-the-ground Radar and Altimeter PIRA was developed and suggested for use in planetary research in 1997 [19]. The PIRA has a penetration depth of more than one kilometer. In 2003, a radio reflection tomography mission to determine the geophysical properties of the deep interior of a near-Earth asteroid was proposed [14].

The first attempt to measure the deep interior structure of a small solar system body was Comet Nucleus Sounding Experiment by Radio-wave Transmission (CONCERT), a part of ESA's Rosetta mission to explore the comet 67P/Churyumov-Gerasimenko, in which a radiotomographic radar signal was transmitted between the orbiter *Rosetta* and the lander *Philae* [35, 36, 37]. Many more missions aiming at exploring the structure and composition of small solar system bodies are currently ongoing. In August 2018, the Osiris-REx mission by NASA [17] will make a rendezvous with the asteroid 101955 Bennu to measure its physical, geological and chemical properties and collect a sample of asteroid regolith on its surface [48] . The Japanese Aerospace Exploration Agency (JAXA) explored the asteroid Itokawa already in 2005 [6] and retreived surface regolith for analysis on Earth [31], and confirmed the Earth-based radar and Hayabusa orbiter measurements

of the classification of the asteroid [41, 42, 55]. The Hayabusa-2 mission by JAXA arrived at the asteroid 16173 Ryugu in mid-June 2018 and will survey the asteroid for a year and a half, returning to Earth in December 2020 [56]. These missions by NASA and JAXA concentrate on surface properties of the asteroids and do not carry instruments which could be used to explore the deep interior of the asteroids.

The next candidate mission to deploy a computed radar tomography system to explore the deep interior of an asteroid is ESA's Asteroid Impact Mission Hera which is due to launch in 2023 [40]. The target of the mission proposal is the binary near-Earth asteroid system Didymos. The current plan would allow for a payload of CubeSat opportunity, consisting of the deployment of two 3U CubeSats [40].

For deployment of CubeSats in computed radar tomography, the concept of Deep Interior Scanning CUbesat (DISCUS) involving bistatic radar measurement has been suggeted and validated numerically [15, 46, 52]. The numerical experiments investigating a mathematical model applied to invert full-wave data for realistic asteroid sizes and shapes suggest that such system can be used to detect macropores from the planned orbiting distance [52].

This thesis extends the work in [52] to study a realistic rubble-pile asteroid model. The realistic refers to the realistic shape, size, material composition and structure of the asteroid. The earlier work is augmented in this work by modelling a realistic internal structure and adding structural details such as void space, a cavity of highly porous material, electrically dense material, and cracks of various shapes and locations, to the realistic, complex shape of the asteroid Itokawa.

The aim of the thesis is to show that the CubeSat mission with bistatic radar instruments described by the DISCUS concept can detect voids, cracks, and boulders inside a realistic asteroid geometry, in realistic environment and conditions.

2. THEORY

2.1 Stepped-frequency ground penetrating radar

2.1.1 Operating principle

The Deep Interior Scanning CubeSat (DISCUS) design [15] carries two identical six-unit (6U) CubeSats as a tandem to form a bistatic radar configuration (Figure 2.1(a)). The stepped-frequency radar transmits a series of narrow-bandwidth pulses stepped by a fixed frequency increase Δf (Figure 2.1(b)). Each series of pulses is referred to as a burst. The receiver samples the signal a rate which coincides to the center of each pulse.

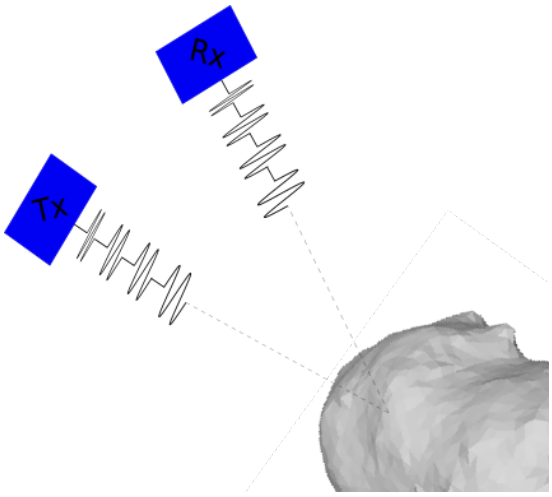

(a) A bistatic stepped-frequency radar configuration with transmitter (Tx) and receiver (Rx).

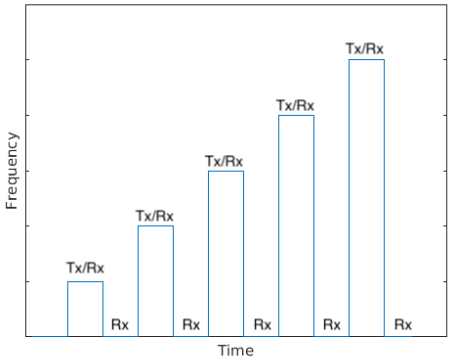

(b) Stepped-frequency pulses. Transmitter (Tx) is active during the pulse and the receiver (Rx) registers signal continuously

***Figure 2.1**. Operating principle of a step-frequency radar. The transmitter (Tx) transmits pulses with increasing frequency. The pulses penetrate the asteroid into the asteroid and the penetration depths is dependent on the pulse frequency and the electromagnetic properties of the asteroid interior. The reflected pulses are captured by the receiver (Rx) which registers the pulse frequency and hence the traveltime of a pulse can be computed.*

The operating principle of the radar relies on the electromagnetic theory and materials' response to electromagnetic waves. Mathematically the physics of the electromagnetic fields are described by Maxwell's equations and expressed as

$$\vec{\nabla} \times \vec{E} = -\frac{\partial \vec{B}}{\partial t} \tag{2.1}$$

$$\vec{\nabla} \times \vec{H} = \vec{J} + \frac{\partial \vec{D}}{\partial t} \tag{2.2}$$

$$\vec{\nabla} \cdot \vec{D} = q \tag{2.3}$$

$$\vec{\nabla} \cdot \vec{B} = 0 \tag{2.4}$$

where $\vec{E}$ is the electric field strength vector (in V/m), q is the electric charge density (in C/m^3), $\vec{B}$ is the magnetic flux density vector (in T), $\vec{J}$ is the electric current density vector (in A/m^2), $\vec{D}$ is the electric displacement vector (in C/m^2), t is the time (in s), and $\vec{H}$ is the magnetic field intensity (in A/m).

The consititutive relationships describe a material's response to electromagnetic fields. In ground penetrating radar applications, the electrical and magnetic properties of the material are of importance. Such constitutive equations provide a macroscopic description on how the material responds to an electromagnetic field. Here, the constitutive equations are

$$\vec{J} = \tilde{\sigma}\vec{E} \tag{2.5}$$

$$\vec{D} = \tilde{\varepsilon}\vec{E} \tag{2.6}$$

$$\vec{B} = \tilde{\mu}\vec{H} \tag{2.7}$$

In the equation 2.5, electrical conductivity $\tilde{\sigma}$ characterizes free charge movement (creating electrical current) in the presence of an electrical field. Such resistance to charge flow leads to energy dissipation. Dielectric permittivity $\tilde{\varepsilon}$ in the equation 2.6 describes the displacement of charge within the material structure in the presence of an electric field. Charge displacement results in energy storage in the material. In the equation 2.7, magnetic permeability $\tilde{\mu}$ describes the intrinsic atomic and molecular magnetic moment response to a magnetic field. For simple materials, distorting intrinsic magnetic moment store energy in the material.

In ground penetrating radar applications, $\tilde{\sigma}$, $\tilde{\varepsilon}$, and $\tilde{\mu}$ are treated as field-independent scalar quantities, which response is in the same direction as the exciting field and is independent of field strength. Furthermore, the frequency of the wave is high enough that the dielectric properties ε, σ and μ of the medium are frequency-independent [13]. Such assumptions simplify computation and appears to be valid in realistic practical applications [13, pp.7]. In most applications the variations in electrical permittivity and conductivity of the material are the most important, while variations in magnetic permeability are seldom

of concern because magnetic properties of rocks and soil are negligible in comparison to their electrical properties.

2.1.2 Interaction of electromagnetic waves with matter

As electromagnetic waves propagate through material they interact with particles and inhomogeneities, locally perturbing the local electron distribution in the matter. Electromagnetic wave interaction produces periodic oscillations of the induced local dipole moments and can act as a source of electromagnetic radiation causing scattering. The majority of the scattered wave oscillates at the same frequency as the incident wave and the scattering is elastic.

Interaction of waves with matter may also lead to absorption in which the energy of the wave is absorbed by the electrons of an atom. Thus the electromagnetic energy is transformed into internal energy of the absorbing material, for example thermal energy.

The combination of scattering and absorption events decreases the intensity of an electromagnetic wave and is referred to as attenuation. Attenuation limits the range of electromagnetic waves and is affected by the materials through which the signal travels. Therefore, when an electromagnetic wave propagates in materials, it is attenuated due to the dielectric and magnetic properties, in other words the composition, of materials.

2.1.3 Electrical permittivity

A body's electrical permittivity describes the material's ability to store and release electromagnetic energy in the form of electric charge. Classically it relates to the storage ability of capacitors. Alternatively, it can be described as the ability to restrict the flow of free charges (in F/m) or the degree of polarisation exhibited by a material under the influence of an applied electric field. In this thesis and many practical applications it is used in terms of a non-dimensional, relative permittivity term ε_r:

$$\varepsilon_r = \frac{\varepsilon}{\varepsilon_0}, \tag{2.8}$$

in which ε is the permittivity of the material and ε_0 is the permittivity of vacuum. The permittivity of the vacuum $\varepsilon_0 = 8.8542 \cdot 10^{-12}$ F/m.

The relative permittivity of a material is directly related to the electric susceptibility (χ_e) of the dielectric material, which is a measure of how easily the material polarizes in response to an electric field, given by

$$\chi_e = \varepsilon_r - 1. \tag{2.9}$$

The permittivity of materials can vary dramatically as a function of porosity, material composition, temperature, internal structure and/or the scale of heterogeneity of structure. The presence of free and bound water increases permittivity easily by an order of magnitude [21, pp.46]. Electrical permittivity is a complex, frequency-dependent quantity with real (energy storage) and imaginary (energy loss) components. It is often, as also in this thesis, simplified to its constant, low-frequency real component with the loss term ignored. This is convenient and possible for the approximate calculation of radar wave velocities and wavelengths, but loses some of the details in the analysis [21].

2.1.4 Radar design and range resolution

The radar signal is generated by the transmitter which supplies an electric current to the antenna. During transmission, the oscillating current applied to the antenna creates and oscillating electric field around the antenna elements. These fields radiate electromagnetic energy away from the antenna into space as a moving transverse electromagnetic field waves. The stepped-frequency radar transmits such series of pulses with increasing frequency.

The radar design is based on the stepped-frequency technique which allows for high effective bandwidth with narrow instantaneous bandwidth, enabling higher signal-to-noise ratio. In comparison to impulse radars, the required peak power is smaller in stepped-frequency radars.

The range resolution δ_r of the radar is dependent on the signal velocity v and the bandwidth B by

$$\delta_r = \frac{v}{2B}. \tag{2.10}$$

In vacuum (free space), signal velocity corresponds to the speed of light c. The speed of signal travelling in a dielectric medium, v, can be derived from Maxwell's equations 2.1-2.4 and is given by

$$v = \frac{1}{\sqrt{\mu\varepsilon}}, \tag{2.11}$$

in which μ is the magnetic permeability of the medium and ε is the permittivity of the medium. By combining equations 2.8 and 2.11, the speed of signal travelling in a dielectric medium is given by

$$v = \frac{1}{\sqrt{\varepsilon_r}} \frac{1}{\sqrt{\mu\varepsilon}}. \tag{2.12}$$

Combining the equations 2.10 and 2.12 yields the equation for range resolution δ_r of the radar in a dielectric medium

$$\delta_r = \frac{1}{\sqrt{\varepsilon_r}} \frac{c}{2B}. \tag{2.13}$$

2.1.5 Radar equation

Radar equation describes the power P_r returning to the receiving antenna

$$P_r = \frac{P_t G_t A_r \sigma F^4}{(4\pi)^2 R_t^2 R_r^2}, \tag{2.14}$$

where P_t is the transmitter power, G_t the gain of the transmitting antenna, A_r the effective aperture (area) of the receiving antenna (which can also be expressed as $G_r \lambda^2/(4\pi)$, in which λ is the transmitted wavelength and G_r is the gain of the receiving antenna), σ is the radar cross section, or scattering coefficient of the target, F is the pattern propagation factor, R_t is the distance from the transmitter to the target, and R_r is the distance from the target to the receiver.

2.1.6 Realistic radargram

The key to understanding ground penetrating radar measurement data is to realize that the image constructed on the screen is not a cross-section of the subsurface but is the time-dependent response of the subsurface materials to the propagation of electromagnetic energy, as recorded at the receiving antenna. The reconstructed radar image is a function of the power of the wave echo recorded by the receiver.

The Figure 2.2 shows a radargram and wave echo power plots produced by the MARSIS (Mars Advanced Radar for Subsurface and Ionosphere Sounding) radar on board of European Space Agency's mission Mars Express, sounding the South Pole of Mars. The reconstructed image shows bright echoes at the surface of the planet and at the interface of the South Polar Layered Deposits (SPLD) and basal material. The echo power plot shows how the power of the received echo is higher than the power of the surface echo along approximately 20 kilometer distance (between the along-track distance 40-60 km. Such bright echo is a result of a material with high dielectric permittivity ($\varepsilon_r > 15$) and strongly suggests the presence of water-bearing materials at a depth of approximately 1.5 kilometers [43].

2.2 Computed radio tomography in asteroid modelling

The computed radio tomography problem is formulated as a far-field model depicted in the Figure 2.3. The 3D asteroid model is fixed to the center of an origo-centric sphere

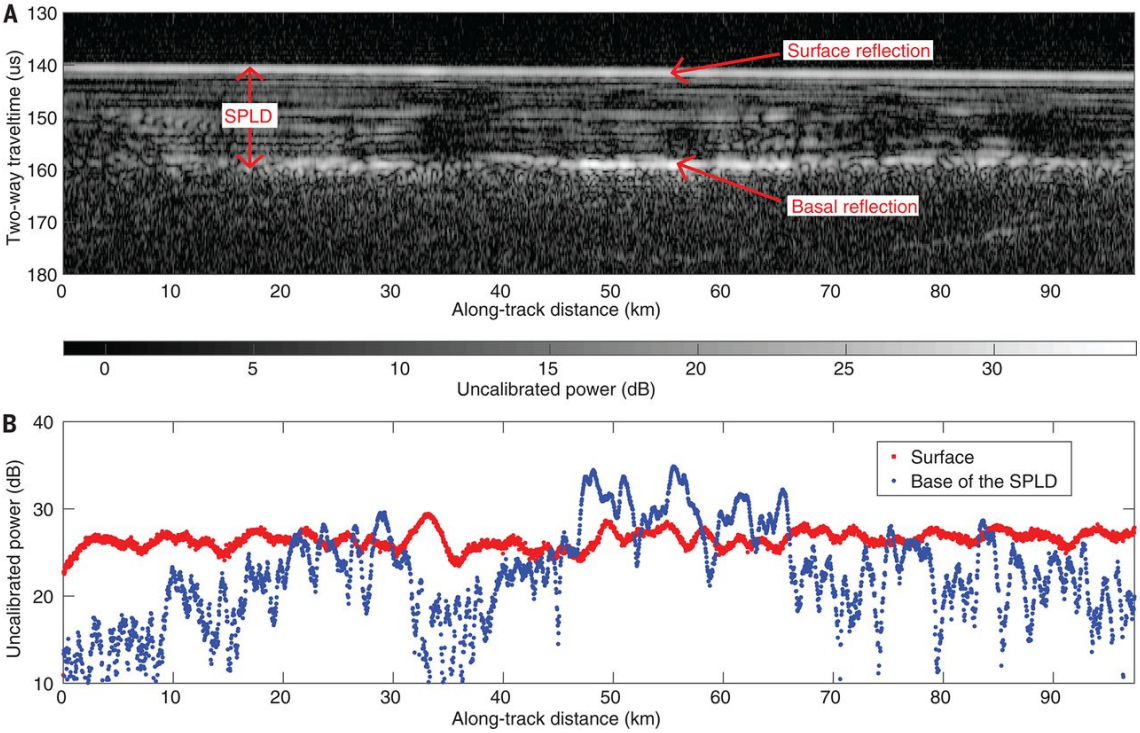

Figure 2.2. *A radargram and echo power plots of the European Space Agency's MARSIS radar showing actual radar measurement data detecting a bright subsurface reflections corresponding to high (>15) electrical permittivity, matching that of water-bearing materials and suggesting liquid wated can be found in the subsurface regions in the South Polar Layered Deposits (SPLD) in the southern ice cap of the planet Mars. [43]*

($\mathscr{S}$) enclosing the domain Ω_2, enclosed in an origo-centric cube (Ω_1), which contains a split-field perfectly matched layer to simulate open field scattering. The satellites carrying the radars are located outside the domain $\Omega = \Omega_1 \cup \Omega_2$. [52]

2.2.1 Satellite points

Satellite points are computed for the bistatic (two-satellite) orbiter configuration as presented in Figure 2.4. The satellite position is presented by spherical coordinates (r, θ, φ), in which the angle θ is the angle between the satellite orbiting plane normal and the asteroid spin, and the angle φ is the angle covered by the satellite due to its motion. The radius, r, is the satellite orbiting distance.

The satellite positions $\vec{p}$ at each time point are determined by the asteroid spin w_1, and the angular frequency with which the satellite orbits the asteroid, w_2. At a time point t, the position of a satellite is determined by

$$\vec{p} = p(t)R_z, \tag{2.15}$$

in which $p(t)$ is the satellite position at time t as determined by the satellite motion, and

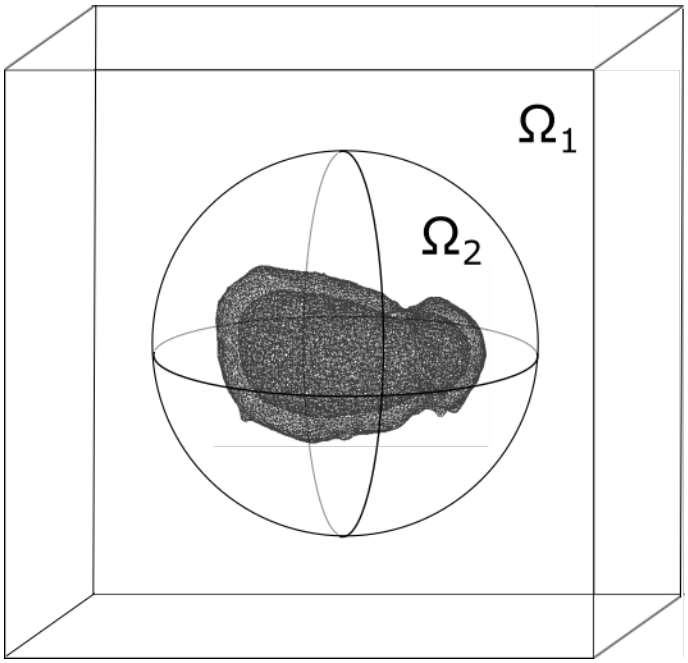

Figure 2.3. *The structure and domains of the computational model (not in scale). The domain* $\Omega = \Omega_1 \cup \Omega_2$. *The interior of the sphere* $\mathscr{S}$ *centered at the origin forms the subdomain* Ω_2. *The exterior of the domain* Ω_2 *inside the cube,* Ω_1, *contains a split-field perfectly matched layer to simulate open field scattering. The asteroid which interior structure is to be modelled is placed inside the sphere* $\mathscr{S}$, *and its origin is aligned with the origin of* Ω_2.

R_z is a rotation matrix around the z axis accounting for the correction in the position due to the retrograde spin of the asteroid. The point $p(t)$ is calculated by

$$p(t) = \begin{bmatrix} \cos(\varphi_2(t) + k\beta)\cos\theta \\ sin(\varphi_2(t) + k\beta) \\ \cos(\varphi_2(t) + k\beta)\sin\theta \end{bmatrix}, \tag{2.16}$$

in which $\varphi_2(t) = 2\pi w_2 t$, accounting for the angular movement of a satellite, $k = 0$ for satellite 1 and $k = 1$ for satellite 2, and β is the bistatic angle between the satellites.

The rotation matrix R_z around the z axis is given by

$$R_z(\varphi_1(t)) = \begin{bmatrix} \cos\varphi_1(t) & -\sin\varphi_1(t) & 0 \\ \sin\varphi_1(t) & \cos\varphi_1(t) & 0 \\ 0 & 0 & 1 \end{bmatrix}, \tag{2.17}$$

in which $\varphi_1(t) = 2\pi w_1 t$ is the angle which is covered due to asteroid rotation.

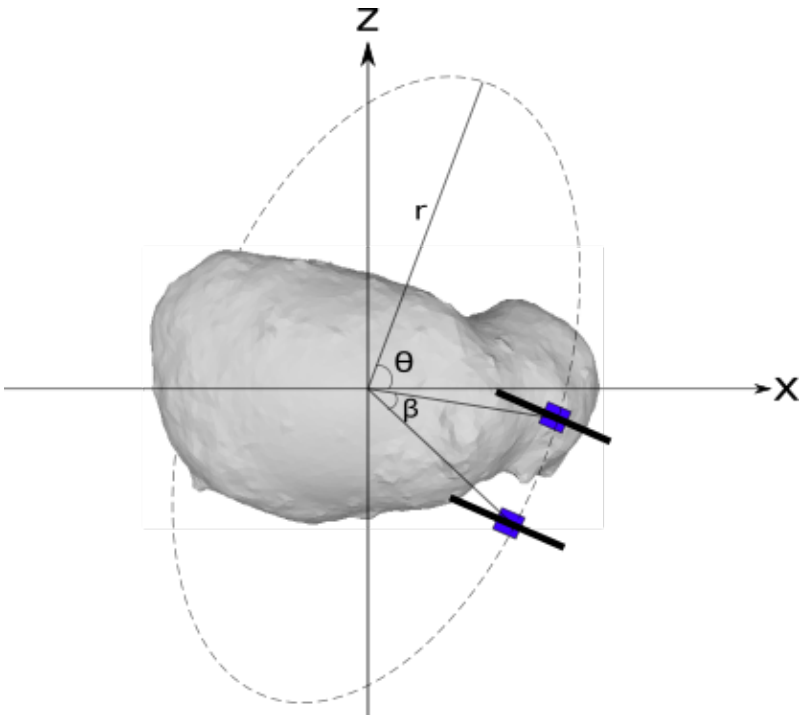

***Figure 2.4**. A schematic illustration of the bistatic measurement approach. The angle θ depicts the limiting angle between the satellite orbiting plane normal and the asteroid spin. The angle β is the angle between the satellites in their orbitting plane. The two satellites orbit at distance r from the center of the asteroid.*

2.2.2 Forward model

The radio signal transmitted at point $\vec{p}$ in a spatio-temporal domain $[0,T]$ is modelled as a point source of the form

$$\frac{\partial f(t,\vec{x})}{\partial t} = \frac{\partial \tilde{f}(t)}{\partial t}\delta(\vec{x}-\vec{p}) \quad \text{with} \quad \tilde{f}(0) = \frac{\partial \tilde{f}}{\partial t}(0) = 0, \tag{2.18}$$

in which $\delta(\vec{x}-\vec{p})$ denotes the Dirac's delta funktion satisfying $\int h(\vec{x})\delta(\vec{x}-\vec{p})dV = h(\vec{p})$ for any sufficiently regular function h.

The resulting electrical potential field u, which is the signal captured by the antenna, is assumed to satisfy the hyperbolic wave equation

$$\varepsilon_r \frac{\partial^2 u}{\partial t^2} + \sigma \frac{\partial u}{\partial t} - \Delta_{\vec{x}} u = \frac{\partial f}{\partial t} \quad \text{with} \quad u(0,\vec{x}) = \frac{\partial u}{\partial t}(0,\vec{x}), \tag{2.19}$$

in which ε_r is the real-valued relative electric permittivity and σ the real conductivity distribution.

The equation 2.19 is solved in its weak form

$$\varepsilon_r \frac{\partial u}{\partial t} + \sigma u - \nabla \cdot \vec{g} = f \quad \text{and}$$
$$\frac{\partial \vec{g}}{\partial t} - \nabla u = 0, \tag{2.20}$$

where $\vec{g} = \int_0^t \nabla u(\tau, \vec{x}) d\tau$ in the domain $\Omega \times [0,T]$.

Solving a partial differential equation such as 2.20 is not straightforward. However, rewriting the equations by multiplying the first and the second equation by test functions $v : [0,T] \to H^1(\Omega)$ ja $\vec{w} : [0,T] \to L_2(\Omega)$, respectively, and transferring partial derivatives to those test functions [46] yields the weak formulation of the problem

$$\frac{\partial}{\partial t} \int_\Omega \varepsilon_r u v d\Omega + \int_\Omega \sigma u v d\Omega + \int_\Omega \vec{g} \cdot \nabla v d\Omega = \begin{cases} \tilde{f}(t), & \text{if } \vec{x} = \vec{p}, \\ 0, & \text{otherwise.} \end{cases} \tag{2.21}$$

$$\frac{\partial}{\partial t} \int_\Omega \vec{g} \cdot \vec{w} d\Omega - \int_\Omega \vec{w} \cdot \nabla u d\Omega = 0 \tag{2.22}$$

Under regular-enough conditions, this weak formulation has the unique solution $u : [0,T] \to H^1(\Omega)$ [29].

The forward model is the discretized, linearized and simulated in a finite element mesh. The details of these methods are described in [46] and [54]. The forward simulation is run to the asteroid model under investigation and a background model.

2.2.3 Inversion process

The forward problem is to predict the voltage of the antenna, given the computation geometry and the unknown parameters. The inversion task is to recover the relative electrical permittivity formulated as

$$\mathbf{L}\mathbf{x} + \mathbf{n} = \mathbf{y} - \mathbf{y}_{bg}, \tag{2.23}$$

where the vectors $\mathbf{y}$ and $\mathbf{y}_{bg}$ contain the measured and simulated data for ε_r and ε_{bg}, respectively. The vector $\mathbf{x}$ is the coordinate vector for ε_r, $\mathbf{n}$ is a noise term including modelling and measurement errors, and $\mathbf{L}$ corresponds to the Jacobian matrix resulting from the linearization [46].

The relative permittivity distribution is reconstructed via the total variation based iteration. An estimate of $\mathbf{x}$ can be obtained via the iterative regularization procedure

$$\mathbf{x}_\ell = (\mathbf{L}^T\mathbf{L} + \alpha\mathbf{D}\boldsymbol{\Gamma}_\ell\mathbf{D})^{-1}\mathbf{L}^T\mathbf{y}, \quad \boldsymbol{\Gamma}_\ell = \mathrm{diag}(|\mathbf{D}\mathbf{x}_\ell|)^{-1}, \tag{2.24}$$

in which $\boldsymbol{\Gamma}_0 = \mathbf{I}$ and $\mathbf{D}$ is of the form:

$$D_{i,j} = \beta\delta_{i,j} + \frac{\ell^{(i,j)}}{\max_{i,j}\ell^{(i,j)}}(2\delta_{i,j} - 1),$$
$$\delta_{i,j} = \begin{cases} 1, & \text{if } j = i, \\ 0 & \text{otherwise [46].} \end{cases} \tag{2.25}$$

The first term is a weighed identity operator limiting the total magnitude of $\mathbf{x}$, whereas the second term penalizes the jumps of $\mathbf{x}$ over the edges of the mesh, the $\ell^{(i,j)}$ being the edge length.

The inversion process in the equation 2.24 minimizes the function

$$F(\mathbf{x}) = \|\mathbf{L}\mathbf{x} - \mathbf{y}_{bg} - \mathbf{y}\|_2^2 + 2\sqrt{\alpha}\|\mathbf{D}\mathbf{x}\|_1, \tag{2.26}$$

in which the second term equals the total variation of $\mathbf{x}$ if $\beta = 0$ [46]. The coefficients α and β are the requlariza tion parameters.

2.3 Gaussian random fields

2.3.1 Multivariate normal distribution

Multivariate standard normal distribution

Definition 2.3.1. A random variable $\mathbf{U} = \{U_1, \ldots, U_k\}$ has a k-dimensional standard normal distribution $N_k(\mathbf{0}, \mathbf{I})$ exactly when its components U_i are independent random variables from the $N(0,1)$ normal distribution.

Due to the independence assumption it follows that the probability density function of the vector $\mathbf{U} \sim N_k(\mathbf{0}, \mathbf{I})$ is

$$f_{\mathbf{U}}(\mathbf{u}) = \prod_{i=1}^{k} f_{U_i}(u_i) = \prod_{i=1}^{k} \frac{1}{\sqrt{2\pi}} e^{-\frac{1}{2}u_i^2}$$
$$= (2\pi)^{-k/2}\exp(-\frac{1}{2}(u_1^2 + \cdots + u_k^2)) = (2\pi)^{-k/2}\exp(-\frac{1}{2}\mathbf{u}^T\mathbf{u}). \tag{2.27}$$

The expectation value of the random variable vector $\mathbf{U}$ is a k-dimensional zero vector and the covariance matrix is a unit matrix of $k \times k$ dimensions

$$\mathrm{E}[\mathbf{U}] = \mathbf{0}_k, \qquad \mathrm{Cov}[\mathbf{U}] = \mathbf{I}_k. \tag{2.28}$$

The moments of the random vector $\mathbf{U}$ are given by

$$M_{\mathbf{U}}(\mathbf{t}) = \mathrm{E}[\exp(t^T\mathbf{U})] = \mathrm{E}\left[\prod_{i=1}^{k}\exp(t_iU_i)\right] = \prod_{i=1}^{k} e^{\frac{1}{2}t_i^2} = \exp(\frac{1}{2}\mathbf{t}^T\mathbf{t}). \tag{2.29}$$

The general multivariate normal distribution

The general multivariate normal distribution can be extended by the definitions of the standard normal distribution, by defining the random variable $\mathbf{X}$ by

$$\mathbf{X} = \mathbf{A}\mathbf{U} + \boldsymbol{\mu}, \tag{2.30}$$

in which $\mathbf{A}$ is a positive semi-definite matrix of size $m \times k$, $\mu \in \mathbb{R}^m$ is a vector of constants, and $\mathbf{U} \sim N_k(\mathbf{0}, \mathbf{I}_k)$. Hence the expectation and covariance of the general multivariate normal distribution are

$$\mathrm{E}[\mathbf{X}] = \boldsymbol{\mu}, \qquad \mathrm{Cov}[\mathbf{X}] = \mathbf{A}\mathbf{I}_k\mathbf{A}^T = \mathbf{A}\mathbf{A}^T. \tag{2.31}$$

The covariance matrix of the random vector $\mathbf{X}$ is denoted by

$$\boldsymbol{\Sigma} = \mathrm{Cov}[\mathbf{X}] = \mathbf{A}\mathbf{A}^T. \tag{2.32}$$

The matrix $\boldsymbol{\Sigma} \in \mathbb{R}^{k\times k}$ is a symmetric and positive semi-definite matrix. Hence it has real, non-negative eigenvalues λ_i and eigenvectors $\mathbf{v}_i$.

The moments of $\mathbf{X}$ is obtained by

$$\begin{aligned} M_{\mathbf{X}}(\mathbf{t}) &= \mathrm{E}[\exp(\mathbf{t}^T\mathbf{X})] = \mathrm{E}[\exp(\mathbf{t}^T(\mathbf{A}\mathbf{U}+\boldsymbol{\mu}))] = \exp(\mathbf{t}^T\boldsymbol{\mu})M_U(\mathbf{A}^T\mathbf{t}) \\ &= \exp(\mathbf{t}^T\boldsymbol{\mu} + \frac{1}{2}\mathbf{t}^T\mathbf{A}\mathbf{A}^T\mathbf{t}) = \exp(\mathbf{t}^T\boldsymbol{\mu} + \frac{1}{2}\mathbf{t}^T\boldsymbol{\Sigma}\mathbf{t}). \end{aligned} \tag{2.33}$$

If the covariance matrix $\boldsymbol{\Sigma}$ is positive definite, the random variable $\mathbf{X} \sim N_k(\boldsymbol{\mu}, \boldsymbol{\Sigma})$ has a probability density function which is given by

$$f_{\mathbf{X}}(\mathbf{x}) = (2\pi)^{-k/2}\big(\det(\boldsymbol{\Sigma})\big)^{-1/2}\exp\bigg(-\frac{1}{2}(\mathbf{x}-\boldsymbol{\mu})^T\boldsymbol{\Sigma}^{-1}(\mathbf{x}-\boldsymbol{\mu})\bigg). \tag{2.34}$$

The requirement of positive definite covariance matrix ensures that the matrix is invertible.

2.3.2 Random fields

Definition 2.3.2. A random field is a finite or real-valued function $X(\mathbf{t},\omega)$ which, for every fixed $\mathbf{t}\in T$ in the parameter set T is a measurable function of $\omega\in\Omega$ in the probability space $(\Omega,\mathscr{F},P)$.

In the definition, the probability space consists of the sample space Ω of sample points ω, a σ-algebra $\mathscr{F}$ dividing Ω into subsets, and a probability measure P assigning probabilities to all members of $\mathscr{F}$. The set Ω contains all possible outcomes and each ω corresponds to a possible outcome of an 'experiment'. The members of $\mathscr{F}$ correspond to events which form a σ-algebra for the assignment probabilities [12].

In the three-dimensional Euclidean space, the parameter set $T=\mathbb{R}^3$. Such random variable is hence $X_{\mathbf{t}} = X(\mathbf{t},\omega)$, when $\mathbf{t}\in\mathbb{R}^3$.

The formal definition 2.3.2 simply means that a random field $X_{\mathbf{t}}$ on $\mathbb{R}^k$ is a function which values are random variables for any $\mathbf{t}\in\mathbb{R}^k$. In this thesis, a Gaussian random field is generated to a complex, realistic asteroid geometry and hence the dimension is here three (3), but any $k>0$ is possible.

A random field is described by its finite-dimensional cumulative distributions

$$F_{\mathbf{t}_1,\ldots,\mathbf{t}_k}(x_1,\ldots,x_k) = \text{Prob}\left\{X_{\mathbf{t}_1}\le x_1,\ldots,X_{\mathbf{t}_k}\le x_k\right\}, \tag{2.35}$$

which are *right-continuous* and *non-decreasing* [12].

The finite-dimensional distributions must satisfy two consistency requirements, the *symmetry condition* and the *compatibility condition*. When we consider a permutation π of the index set $\{1,\ldots,k\}$, we see that the events $[X_{\mathbf{t}_1}\le x_1,\ldots,X_{\mathbf{t}_k}\le x_k]$ and $[X_{\mathbf{t}_{\pi 1}}\le x_{\pi 1},\ldots,X_{\mathbf{t}_{\pi k}}\le x_{\pi k}]$ are identical. Hence, the *symmetry condition*

$$F_{\mathbf{t}_1,\ldots,\mathbf{t}_k}(x_1,\ldots,x_k) = F_{\mathbf{t}_{\pi 1},\ldots,\mathbf{t}_{\pi k}}(x_{\pi 1},\ldots,x_{\pi k}) \tag{2.36}$$

must hold. A similar argument implies that the *compatibility condition*

$$F_{\mathbf{t}_1,\ldots,\mathbf{t}_{k-1}}(x_1,\ldots,x_{k-1}) = F_{\mathbf{t}_1,\ldots,\mathbf{t}_{k-1},\mathbf{t}_k}(x_1,\ldots,x_{k-1},\infty) \tag{2.37}$$

must be satisfied. These two conditions 2.36 and 2.37 need to be satisfied by cumulative distribution functions (2.35) originating from a random field.

The expectation of a random field is by definition

$$m(\mathbf{t}) = \mathrm{E}[X_{\mathbf{t}}] = \int_{\Omega} X_t(\omega) dP(\omega). \tag{2.38}$$

The covariance function is expressed as

$$C(\mathbf{t},\mathbf{s}) = \mathrm{Cov}[X_{\mathbf{t}}, X_{\mathbf{s}}] = \mathrm{E}[X_{\mathbf{t}} X_{\mathbf{s}}] - m(\mathbf{t})m(\mathbf{s}), \tag{2.39}$$

and the variance is

$$\sigma^2(\mathbf{t}) = C(\mathbf{t},\mathbf{t}). \tag{2.40}$$

The autocorrelation function of a random field is by definition

$$\rho(\mathbf{t},\mathbf{s}) = \mathrm{Corr}[X_{\mathbf{t}}, X_{\mathbf{s}}] = \frac{C(\mathbf{t},\mathbf{s})}{\sigma(\mathbf{t})\sigma(\mathbf{s})}. \tag{2.41}$$

Definition 2.3.3. A Gaussian random field is a random field where all the finite-dimensional distributions, $F_{\mathbf{t}_1,\ldots,\mathbf{t}_k}$, are multivariate normal distribution for any choice of k and $\{\mathbf{t}_1, \ldots \mathbf{t}_k\}$.

A random field can be described further by its stationary and isotropic or anisotropic properties. The strict definition of stationarity requires that all its finite-dimensional distributions are invariant under arbitrary translations. In the following, we assume that T is a linear space such that $\mathbf{t},\mathbf{s} \in T$ and that $\mathbf{t}+\mathbf{s} \in T$. The space has a properly defined distance measure or norm, denoted by $d(\mathbf{t},\mathbf{s})$. A typical example of such space would be $\mathbb{R}^n$ with the Euclidean norm $\tau = d((\mathbf{t},(\mathbf{s}) = \|\tau\| = \sqrt{\tau_1^2 + \cdots + \tau_n^2}$.

Definition 2.3.4. (**Stationarity in the wide sense**) A random field is a *stationary random field* if

$$m(\mathbf{t}) = m \qquad \text{and} \qquad C(\mathbf{t},\mathbf{s}) = C(\tau), \tag{2.42}$$

where $\tau = \mathbf{t} - \mathbf{s}$ is the separation vector. The corresponding covariance/correlation function is called a *stationary covariance/correlation function*.

Any stationary covariance function must have constant variance so that $C(\tau) = \sigma^2\rho(\tau)$.

Stationarity implies that the correlation function is translation invariant. A subclass of stationary functions is isotropic functions.

Definition 2.3.5. (**Isotropic random fields**) A stationary random field is an *isotropic random field*, if the covariance function depends on the distance alone, i.e. $C(\mathbf{t},\mathbf{s}) = C(\tau)$, where $\tau = d(\mathbf{t},\mathbf{s})$

Isotropic correlation functions are significant because they are simple: it depends on a single variable, the distance between $\mathbf{t}$ and $\mathbf{s}$. When using a Euclidean norm in $\mathbb{R}^n$, the verification of positive definiteness is simple.

Anisotropic random fields are random fields which stationary correlation function depends on $\boldsymbol{\tau}$ through a non-Euclidean norm of a more general form, such as $\tau = \|\boldsymbol{\tau}\|_{\mathbf{K}} = \sqrt{\boldsymbol{\tau}^t \mathbf{K} \boldsymbol{\tau}}$. The matrix $\mathbf{K}$ must be positive semi-definite to ensure $\|\boldsymbol{\tau}\|_{\mathbf{K}} \geq 0$ for any $\boldsymbol{\tau}$.

A thorough theoretical review of Gaussian random fields is available in [12].

2.4 Graphics Processing Unit computing

Computing applications have traditionally been performed by the central processing unit (CPU). For 30 years, Moore's law of microprocessor performance improvement ensured CPU computing performance grew at a rate of 50 percent per year. However, the limits of semiconductor physics mean that CPU performance grows now only by 10 percent per year. [1]

Graphics Processing Unit (GPU) was originally developed and used to handle and accelerate computations for computer graphics rendering. Such graphics applications usually involve vectors and matrices in two, three or four dimensions. Therefore a typical GPU comprises a massively parallel array of integer and floating-point processors, including a dedicated high-speed memory. As scientific calculations and systems are commonly characterized with large matrix operations, GPUs are increasingly applied to scientific calculations. It is expected that GPU computing extends Moore's law and promises to continue the 50 percent yearly rate of computing performance increase at least up to the year 2025. [4]

The power of GPU computing in especially evident in computationally intensive applications, such as solving partial differential equations in a large system. The limitations of GPU involve memory access, because data has to be sent from the CPU to the GPU before calculation and then retrieved back afterwards [4]. Hence the overall computational speed-up is limited by the amount of data transfer which occurs during the algorithm. Therefore, the computations performed on a GPU need to be

1. computationally intensive, and
2. massively parallel.

This means that the time spent on computation should exceed the time spent on transferring data to and from GPU memory, and the computations should be possible to break

down into hundreds or thousands of independent units of work. The forward model of full-wave simulation (section 2.2.2) used in thesis is a classical example of such application which benefits remarkably from GPU computing.

3. ASTEROIDS

3.1 Small solar system bodies

Asteroids are small, irregularly shaped solar system bodies composed of minerals and rocks. Asteroid and cometary populations of today are the only remnants from the era approximately 4.5 billion years ago, when the large planets in our solar system were formed. Although altered by numerous collisions, internal heating and space weathering, asteroids still represent the least altered material from this time. There are between 1.1 and 1.9 billion asteroids with diameters over 1 kilometer [9] in the so-called main asteroid belt located between the orbits of Mars and Jupiter.

The Near-Earth asteroids (NEAs) are asteroids which orbits pass close (perihelion distance less than 1.3 AU) to that of Earth. To date, more than 18 000 NEAs have been discovered [2]. More than half of them are smaller than 140 meters in size. The size of over 8 000 NEAs is between 140 m and 1 kilometer. Only a vast minority, less than 900 asteroids, are larger than 1 kilometers in size.

Asteroids are classified into groups based on their color, albedo and spectral shape, corresponding to the asteroid's surface material. The original classification system [24] had three categories: C-types for dark carbonaceous objects (75 % of known asteroids), S-type for stony (silicaceous) objects (17 % of known asteroids) and U for the unknown type of asteroids, which did not fit to either the type C or type S. Also other classification systems [53] have been developed and the original spectrum-based system expanded [20] to include a third broad category X into the classification system, which includes, for example, M-type asteroids thought to indicate a metallic body.

3.2 Rubble pile asteroids

A rocky body can be monolithic, fractured or a rubble pile. A monolithic body is relatively uniform in density and contains practically no macroscopic voids or cracks. Its strength is determined by the material itself. Most asteroids, however, are not monoliths, but consist of smaller fragments bound together by gravity. They may contain irregularly shaped crack and voids between the numerous fragments. Such bodies are called rubble piles.

Rubble pile asteroids exhibit high macroporosity which can be explained by void space between fragments [31]. They have been found to have an upper limit to their spin rates [45], providing evidence that asteroids larger than a few hundred meters are mostly loosely bound, gravity-dominated aggregates with negligible tensile strength.

3.3 Itokawa

Asteroid Itokawa is an S-type Near-Earth Asteroid consisting mostly of iron and magnesium rich silicates olivine and pyroxene [31]. A petrological analysis groups it together with ordinary chondrites of subtypes LL4-LL6 [41], and mineral chemistry indicates that the majority of regolith surface particles suffered long-term thermal annealing and subsequent impact shock, suggesting that Itokawa is made of reassembled pieces of the interior portions of a once larger asteroid [55].

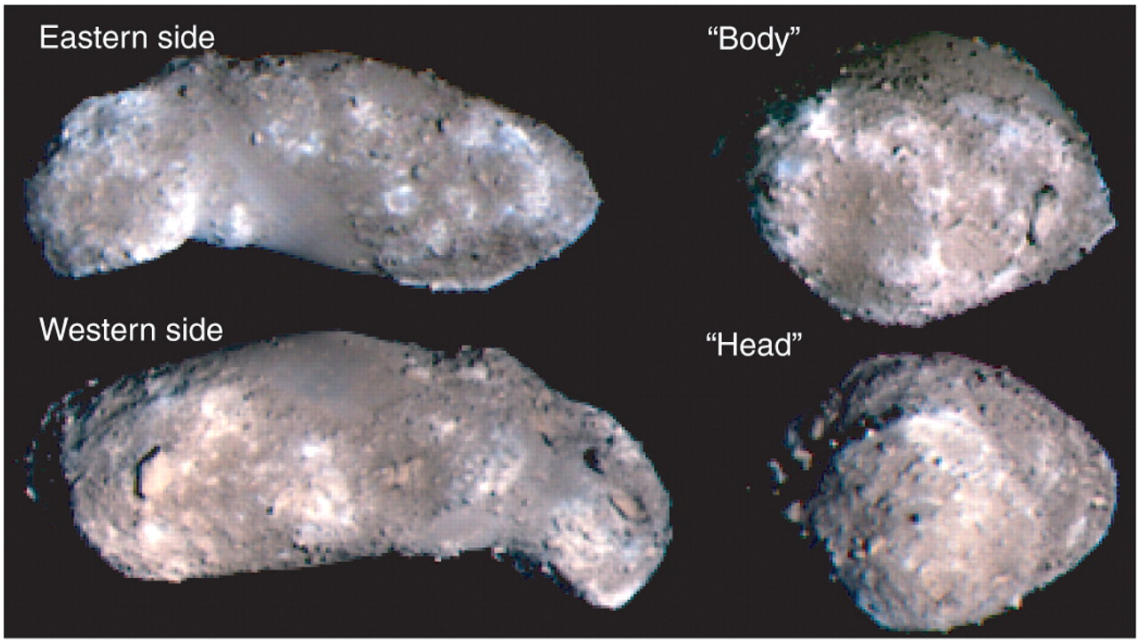

Figure 3.1. *The shape of asteroid Itokawa resembles sea otter. Picture was taken on the Japanese Aerospace Exploration Agency mission Hayabusa. [49]*

Itokawa has a peculiar shape which has been described to resemble a sea otter (Figure 3.1). It is composed of two parts, the smaller one is named the otter's "head" and the other (larger) is the otter's "body". The general appearance of the shape is rounded. The asteroid's orthogonal axes are 535 (x), 294 (y) and 209 (z) meters, the mass is $3.51 \cdot 10^{10}$ kilograms, and the volume approximately $1.87 \cdot 10^7$ m^3 [11]. The estimated bulk density is hence 1.9 ± 0.13 grams per cubic centimeter which is significantly less than S-type asteroids on average (approximately 2.6 g/cm^3). Furthermore, the rotational period of Itokawa is 12.1 hours [31]. The measured values for bulk density leading to macroporosity and rotational period both make a strong suggestion that Itokawa is a rubble pile asteroid.

Macroporosity of Itokawa was estimated to be approximately 41 percent, whereas the typical macroporosity of an S-type asteroid is roughly 30 percent. Also the density of ordinary LL chondrites is almost 50 percent higher than the bulk density of Itokawa, suggesting Itokawa contains considerable amount of void space in its interior. It is not yet clear what the relative micro- and macroporosity values are, but at least in terrestial geology, porosities larger than 30 percent commonly indicate loose soils or rubble. [31]

The surface of Itokawa is divided into areas of rough and smooth terrain (Figure 3.2). The rough terrain consists mainly of numerous boulders and the smooth areas of the Muses sea extends around the ”neck” of the asteroid. There is no substantial difference in mineralogical composition over the asteroid’s surface in spite of the bifurcated appearance of Itokawa’s shape [11, 42].

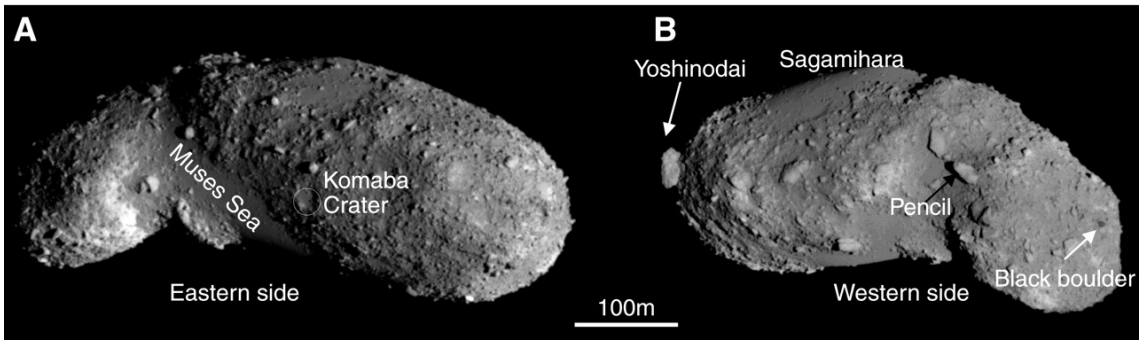

Figure 3.2. *Itokawa as photographed by Hayabusa. There are numerous boulders, such as the labeled Yoshinodai, Pencil and the Black boulder, on the surface of the asteroid. The crater Komaba is also visible, as are the smooth areas of the Muses Sea and Sagamihara. [49]*

Based on the surface images, Itokawa seems to be composed of 100-200 m blocks and to be covered by a thin regolith layer mainly composed of gravels and pebbles [16]. The blocks may be monolithic or an aggregate of smaller blocks, pebbels or gravels and the internal structure can be a complicated network of such smaller bodies. In 2008, Scheeres and Gaskell suggested [50] that non-uniform mass distribution could explain the non-detection of the YORP effect on Itokawa. The YORP effect changes the rotation state of a small astronomical body due to scattering of solar radiation off its surface and the emission of the body’s own thermal radiation. A later study [39] suggested mean densities of 1.75 ± 0.11 g/cm^3 and 2.8 ± 50 g/cm^3 for the two components forming the asteroid. This would imply a rubble pile lobe is attached to a monolithic lobe. Nevertheless, there are also other alternative explanations for the discrepant data, which motivates the need for direct measurements [33].

Electrical permittivity is a function of several properties: porosity, composition of the material, temperature, internal structure, and/or scale of potential heterogeneities. For Itokawa we have reasonable real data for porosity, composition of the material and temperature. Electrical permittivity values of rocky materials found on Earth appear to exhibit some correlation with density. Compact rocks with little porosity are typically represented by values $3 < \varepsilon_r < 10$ [13]. Highly porous materials exhibit smaller permittivity values. The estimated relative electrical permittivity of and S-type asteroid with LL chondrites and with approximately 40 % porosity is 4 [33]. The higher the metal content, the higher the relative permittivity and the value also increases with decreasing porosity.

4. METHODS

4.1 Finite element model of the asteroid Itokawa

The realistic finite element model of the asteroid Itokawa (Figure 4.1) was constructed based on the detailed surface stereolitography file [5] which was further processed to obtain a computationally valid surface model of the asteroid. The unstructured triangulated asteroid surface was imported to Meshlab [27] and resampled with Poisson-disk sampling algorithm to construct a uniform mesh which contained 5 762 nodes and 11 520 faces.

The interior model of the asteroid was constructed from the outer surface model. The interior surface was first smoothed with Laplacian smoothing algorithm to even out the contour. Then the surface was scaled by factor of 0.9. The interior surface was resampled and a uniform mesh was reconstructed by a process similar to the reconstruction of the outer surface. By placing the interior surface inside the asteroid outer surface, a model with surface layer and a surface containing the deep interior of the asteroid was formed. Further details to the deep interior was added by making an ellipsoidal mesh which was placed within the asteroid. The details of constructing the finite element mesh are described in [54].

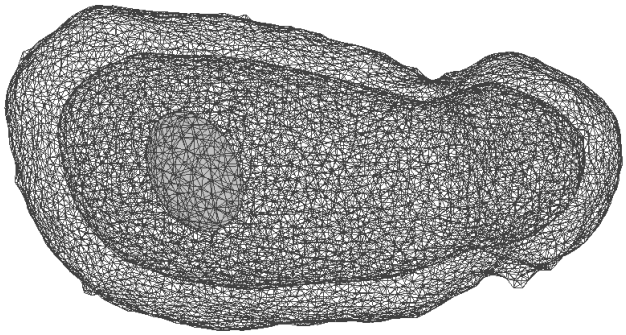

Figure 4.1. *Finite element model of Itokawa including a single deep interior void in the body of the asteroid. The detailed model includes the outer surface of the asteroid, enclosing the interior enclosing a deep interior void.*

4.2 The structure and the domains of the computational model

The structure and the domains of the computational model depicted in Figure 2.3 were constructed in Gmsh [32]. The developed `.geo` scripts describe each surface and volume of the model and thus assign boundaries to the parts of the model, namely the outer cube,

the sphere, and details of the asteroid structure, including the asteroid outside surface, interior surface and deep interior anomalies.

The three-dimensional finite element mesh was computed and optimized by Gmsh tools and stored in `.msh` file from which the mesh node and tetrahedra data were extracted by standard bash script methods. The realistic base model without deep interior details included 37 723 nodes and 212 828 tetrahedra.

4.3 Computing the orbiter points

The data points at which tomography signal is transmitted and received by the orbiters were calculated for the case where there are two orbiters which cover a sparse limited-angle measurement (shown in Figure 2.3). The angle θ between the measurement plane normal and the asteroid spin is 70°. In total 64 measuremet points were included in the point cloud. The parameters for computation is shown in the table 4.1.

Table 4.1. *Parameters for the orbiter tomography signal transmission and receiving point computation, shown schematically in Figure 2.4.*

Parameter	Value
data points	64
n of orbiters	2
r, orbit radius	2.4
θ	70°
bistatic angle, β	25°
asteroid spin rate, w_1	10
orbiter angular frequency, w_2	0.336
traveltime between points, t	0.0175

A quiver plot showing the position and orientation of the two orbiters is in the Figure 4.2. The aperture around the z-axis is evident in the figure

4.4 Computing Gaussian random field inside a realistic asteroid geometry

A computational pipeline to create a Gaussian random field to model a realistic spatial distribution of electrical permittivity inside any realistic asteroid geometry was developed. A Gaussian random field was first generated in a regular three-dimensional meshgrid cube. The mean of the random field was set to 4 and standard deviation of 1. Correlation was chosen to be isotropic. Correlation value was set to 0.2 and was so chosen based on visual examination in order to obtain slight correlation of values, and not totally random Gaussian variation of electrical permittivity inside the cube. This choice was thought to account for the realistic case where an asteroid is composed of materials of variable shapes and sizes bound together by gravity. A completely random (zero-correlation) would have been appropriate for generating a mere noise model.

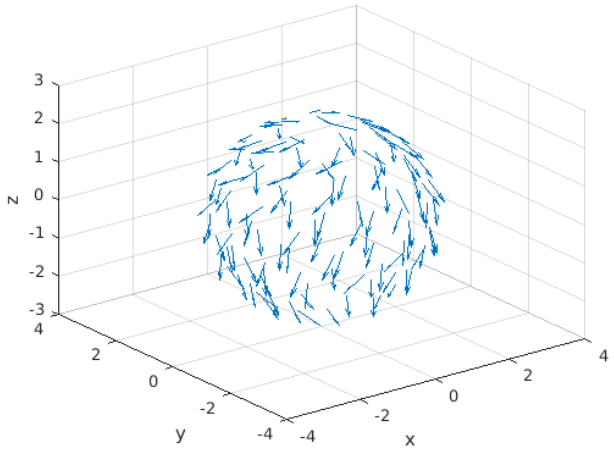

Figure 4.2. *A quiver plot of the orbiter points and orientations around the asteroid.*

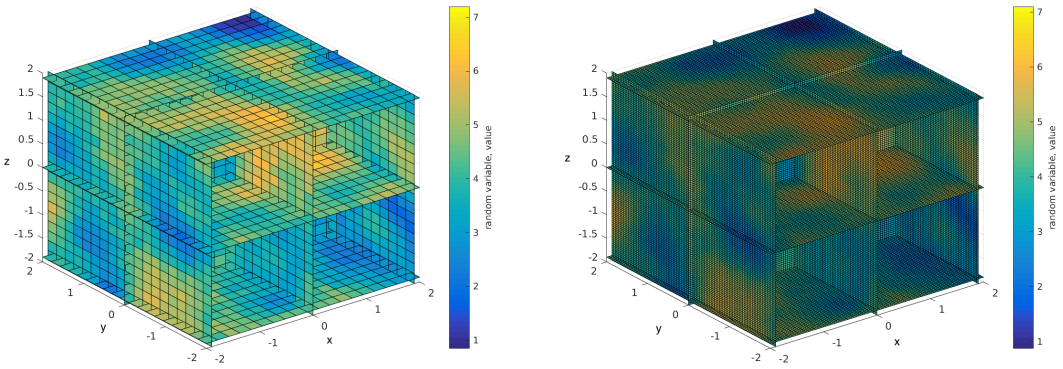

(a) The coarse mesh with Gaussian random field.

(b) The fine mesh with the original Gaussian random field interpolated to the finer mesh.

Figure 4.3. *Generation of the gaussian random fields inside three-dimensional meshgrids.*

The random field was first generated in a coarse mesh, 20 units in each dimension (Figure 4.3(a)). Implementation of the Gaussian random field algorithm was retrieved from [28]. In the next stage, a finer mesh of 100 units per dimension was constructed and the random field values interpolated from the coarse to finer mesh (Figure 4.3(b)). Finally, the realistic asteroid interior geometry was fitted inside the finer cubic mesh and the values in the cubic mesh were assigned to the geometry by mapping the nearest mesh coordinate and its value to the nodes in the realistic asteroid finite element model (Figure 4.4).

Each finite element mesh tetrahedra are assigned a value which is the average of the electrical permittivities of each node constituting the element. Lastly, should the random field have created permittivity values below 1 (which is the electrical permittivity of vacuum and therefore the physical minimum of permittivity), such values are replaced by 1. Figure 4.5 shows cross-sections of asteroid Itokawa interior finite element permittivity mesh

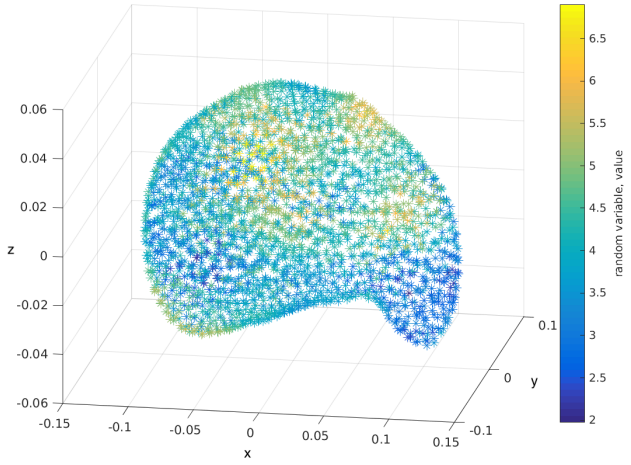

Figure 4.4. *Gaussian random field modelling a realistic asteroid interior. Electrical permittivity values are first interpolated to mesh nodes.*

obtained with the procedure. For each of the following structural models, the Gaussian random field was simulated independently.

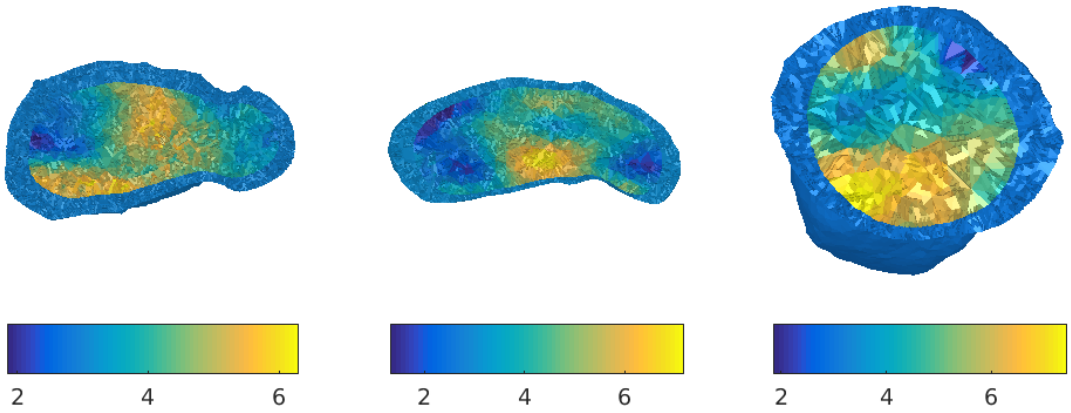

Figure 4.5. *The realistic asteroid interior simulated for each of the deep interior structural models in this thesis. The surface layer is clearly visible and the Gaussian random field in the deep interior models inhomogeneities of the interior.*

4.5 Structural details to the realistic asteroid model

4.5.1 Single small void

The realistic asteroid model was further extended to include a single anomaly in the deep interior. The anomaly was modelled with an ellipsoid placed in the body of the asteroid (Figure 4.6). The anomaly represents a void inside the deep interior of the asteroid. It would correspond to a cavity, for example between two large boulders constituting a part of the body of the asteroid.

Also in this model, the other parts of the interior was modelled with a Gaussian random field to account for the variability of electrical permittivity inside the asteroid due to the rubble-pile nature of the asteroid (Figure 4.6). The model shows how the surface layer of the asteroid is clearly visible and the permittivity values in the interior of the asteroid vary between approximately two to six.

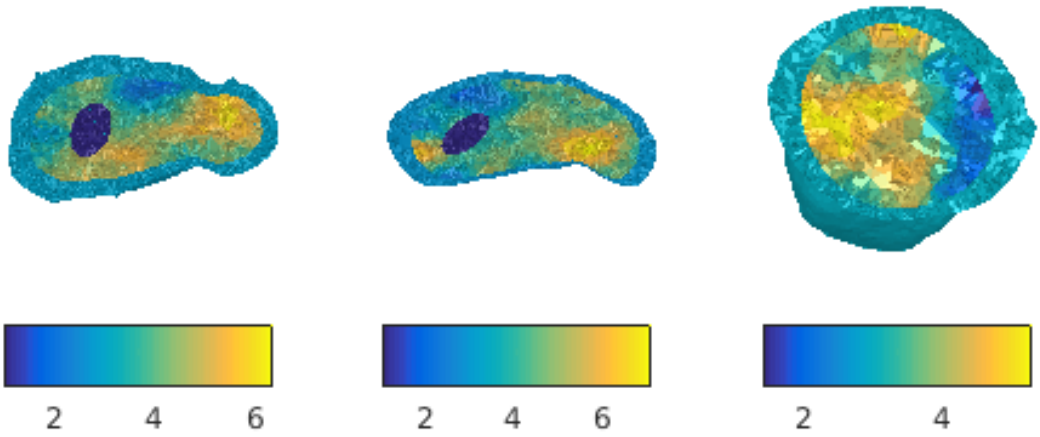

Figure 4.6. *Electrical permittivity model of Itokawa with a single void in the deep interior of the asteroid.*

4.5.2 Single cavity filled with highly porous material

Having empty void space within an asteroid is an interesting case. However, in a realistic case, an asteroid may contain internal structure which dielectric properties are not as distinct from the surroundings as that of having empty void space. Asteroid interior may include not only void space, but also areas which are occupied by a very porous, loose material. Such case is modelled with an ellipsoid shape which electrical permittivity is adjusted to 2 instead of void permittivity (Figure 4.7). The aim of this test case is to model a situation in which there is a larger area of a single substance, but which electrical properties are not as distinct from the surrounding materials as that of a void space.

4.5.3 Single boulder

An asteroid may also be formed around a single large boulder with electrical permittivity significantly higher than that of the surrounding more porous material. Such system is investigated with a model similar to the single void, but the electrical permittivity of the enclosed ellipsoid within the deep interior is assigned a value significantly higher than the surrounding other material (Figure 4.8). Here we chose to fix the ”boulder’s” relative electrical permittivity to 15, corresponding to fractured and wet granite and various types of wet concrete [21], or metallic materials within rocks. Although wet materials are not expected to be found in asteroids, it is important to simulate whether detection of significantly higher relative permittivities is possible.

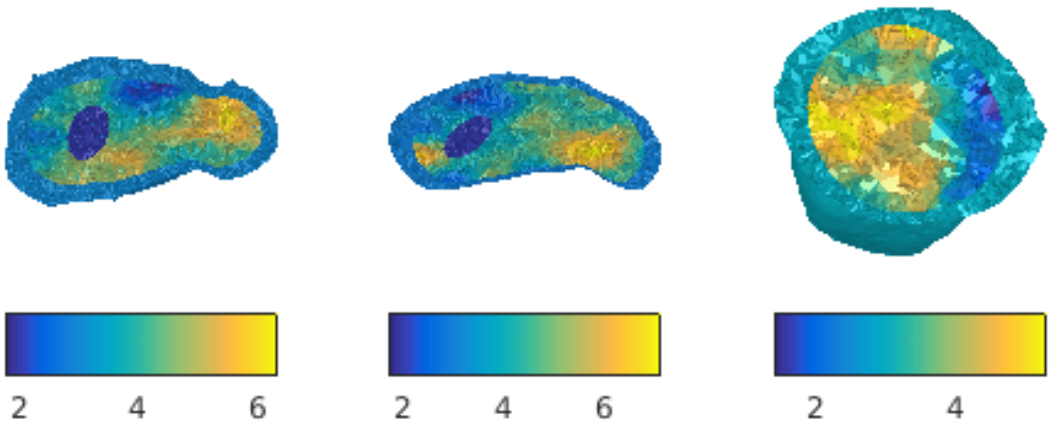

Figure 4.7. *Electrical permittivity model of Itokawa with a cavity with loose and porous material in the deep interior of the asteroid. The structure of the model is the same as in the Figure 4.6, but the permittivity of the cavity is higher than void, adjusted at* $\varepsilon_r = 2$.

4.5.4 Crack in the deep interior

To model a crack inside an asteroid, a simple nearest-neighbour walking algorithm through the finite element mesh nodes was implemented to create a crack across the asteroid interior. At each iteration round the forward step is taken to the next dimension so that the walk iterates to the closest next point in the order $x \to y \to z \to x \to \ldots$. The starting point of the iteration is the median value of the x coordinates. The length of the crack was assigned 100 steps.

Each node which was included in the path was assigned a permittivity value of vacuum. Each tetrahedra was assigned a permittivity value which was average of the permittivities of the constituting nodes. Hence the crack was extended to the finite element mesh.

A crack is irregularly shaped and smaller in comparison to a void (Figure 4.9), therefore more challenging a test for the radar detection power. The obtained crack width is in the order of 5-20 meters, depending on the location within the asteroid.

4.5.5 Shallow crack

A shallow crack was simulated similar to the deep crack (Section 4.5.4), but the selected starting point was the minimum of the x-coordinate of the deep interior of the asteroid model. A similar nearest neighbour walking algorithm was used to select the nodes which were included in the crack. The crack was allowed to form a crossing in approximately the middle of the crack, forming two arms to the crack. Cracks such as these would form between larger boulders due to variable shapes and sizes and therefore detection of such empty space between denser material is of special interest.

The generated shallow crack is depicted in the Figure 4.10. The 3D representation of the

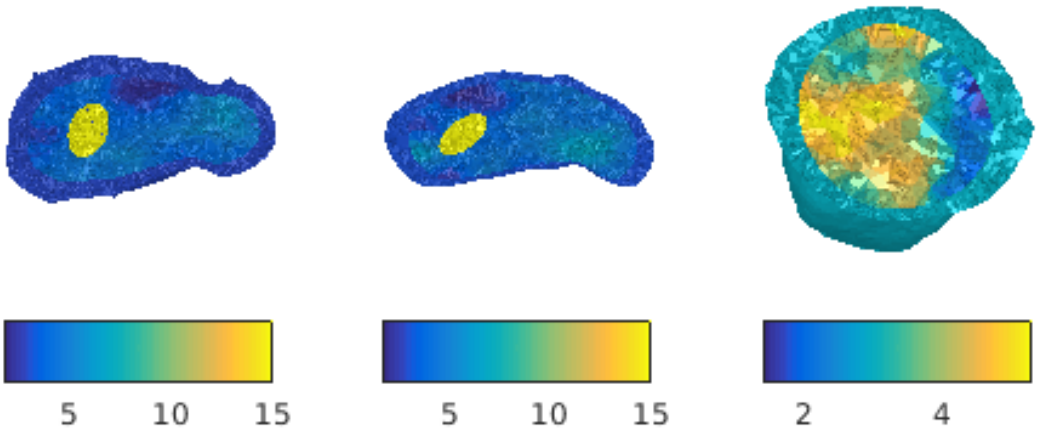

***Figure 4.8**. Electrical permittivity model of Itokawa with a single large boulder with relative electrical permittivity of 15 in the deep interior of the asteroid. Note that the scale of the colormap is different from the other figures in this section due to the high permittivity value of the boulder.*

generated crack is shown in the Figure 4.10(a) and the resulting complete asteroid model is shown in the Figure 4.10(b).

A shallow crack such as this one could be created in the interface of two layers of materials. Because the crack is near the surface of the asteroid, it should be detected by the DISCUS radar.

4.5.6 Background model

Inversion process requires a reference level, a background model, which lacks the detail to be recovered by the simulation. Such background model is constructed similar to the actual computational model (the complete model in the Figure 2.3), but only the outer surface of the asteroid (Figure 4.1) is included in the asteroid model.

The background model finite element mesh is coarse in comparison to the realistic asteroid models including details in the asteroid interior. The electrical permittivity of the background model asteroid is set to a constant value 4. It does not have surface layer or any of the other details.

4.6 Computation parameters

4.6.1 Signal pulse

The signal pulse, $\tilde{f}(t)$, is modelled by a single Blackman-Harris window

$$\tilde{f}(t) = 0.359 - 0.488\cos\left(\frac{2\pi t}{T_0}\right) + 0.141\cos\left(\frac{4\pi t}{T_0}\right) - 0.012\cos\left(\frac{6\pi t}{T_0}\right) \qquad (4.1)$$

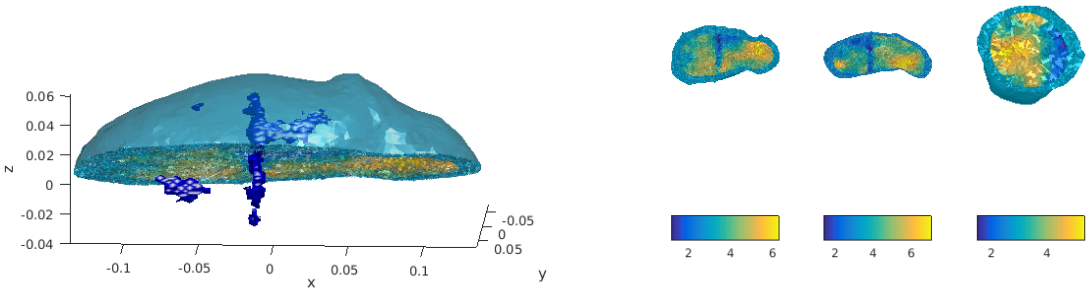

(a) 3D illustration of a deep crack (blue) inside the asteroid interior. Only one half of the asteroid is shown for reference.

(b) The electrical permittivity mesh of Itokawa with a crack in the body of the asteroid.

Figure 4.9. *The generated crack dissects the asteroid interior in the direction of the z axis.*

Table 4.2. *Targeted DISCUS radar parameters [15].*

Center frequency	20-50 MHz
Antenna length	two times 1.5-3.75 m (half-λ)
Radar modulation	32 to 2048 lines
Pulse duration (at 5 kms distance)	32 μs
Pulse repetition time (at 5 kms distance)	150 μs
Input/transmitting power	40 W/10 W
Receiver bandwidth	2 MHz

for $t \in [0, T_0]$ and $\tilde{f}(t) = 0$ otherwise. The unitless pulse duration T_0 was chosen to be 0.12, resulting into approximately 2 MHz bandwidth needed for transmitting the pulse.

4.6.2 Radar specifications

The goal of the DISCUS mission is to include a radar with a 2 MHz total signal bandwidth and 20-50 MHz center frequency [15]. The targeted frequency is in the lower end of usable frequencies and has been selected in order to achieve appropriate signal penetration and to minimize solar noise [34]. Should the Sun be active during measurements, the dominating error source would be the electromagnetic noise originating from solar radiation. The effect of the Sun's radiation is also minimized by pointing the antenna towards the Sun during the measurements in order to minimize capture of any signal from the Sun. The targeted radar parameters are summarized in Table 4.2.

The duration of a single frequency line is given by $\tau = 1/B_\ell$, in which $B_\ell = B/N$, meaning that the total bandwidth B is divided by the number N of frequency lines. Approximately 64 lines with pulse duration 32 μs can be transmitted and received separately from a 5 km distance of the asteroid (the pulse duration is 96 % of the total travel-time) [15].

The minimum distance between separable items discerned by the DISCUS radar is 20 to

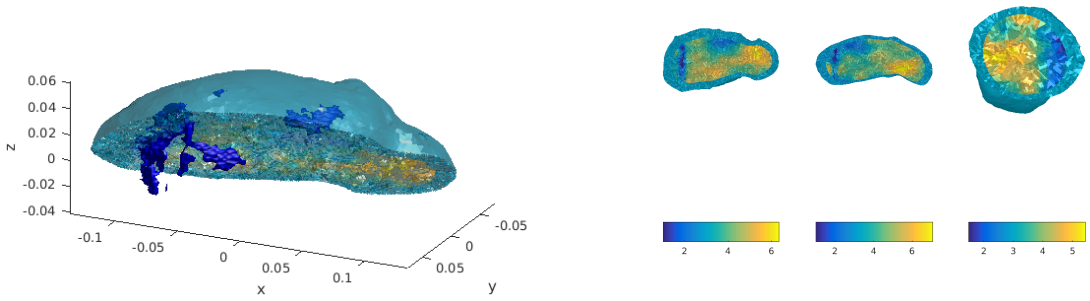

(a) The 3D illustration of the crack (blue) inside the asteroid. The generated crack is shown in blue. A part of the asteroid is shown for reference of the location and size of the crack.

(b) The electrical permittivity mesh of Itokawa with a shallow crack placed at the interface of the surface layer and the deep interior.

Figure 4.10. *The generated shallow crack runs close to the surface layer of the asteroid. It forms two arms, which are clearly shown in the 3D representation of the model, and exhibits a curved shape just below the surface layer of the asteroid.*

40 meters inside the asteroid. The exact range resolution depends on the relative electrical permittivity by the equation 2.13. The lower end of the range is achieved in the areas of high relative permittivity, and the higher end when the relative permittivity is approximately 3. The range resolution in vacuum, for example the deep interior void space, is 75 meters and in the highly porous cavity with relative permittivity of 2 approximately 53 meters.

4.6.3 Noise

The measurement errors in the system are assumed to be mainly caused by the galactic background noise and the radiation from the Sun. The minimum total effect of these corresponds to approximately 20 ± 5 MHz since the galactic noise increases towards the low frequencies.

The noise in the system are contained by the term $\mathbf{n}$ in the equation 2.23, and it is assumed to be Gaussian noise with standard deviation of -11 dB with respect to the maximal entry of the difference $\mathbf{y} - \mathbf{y}^{(bg)}$ between the measured and simulated signal. Such value was selected from the range of simulated values between -25 and 0 dB, reported in [52].

4.7 Computational framework and resources

The computational routine to simulate orbiter-to-orbiter tomography has been initially reported in [46] and later discussed in [52] as implemented to another asteroid geometry. This framework was recently used in a simple deep interior model of the asteroid Itokawa [54]. The computational model has since been extended by Asst. Prof. Pursiainen to account for polarization of the radar antenna (unpublished).

The computationally intensive part of the simulation was run in the GPU partition of Tampere Center for Scientific Computing (TCSC) Narvi cluster which consists of 8 GPU nodes with 20 CPU cores, 4 GPU each, totalling 32 NVIDIA Tesla P100 16 GB GPUs. The inversion reconstruction procedures were run on a Lenovo P910 workstation equipped with two Intel Xeon E5 2697A 2.6 GHz 16-core processors and 128 GB RAM.

Computation of wave propagation in the forward model is highly parallelizable because each of the points transmitting the signal is independent of others. For practical SLURM queue management reasons the computation was parallelized to 16 processes, each computing four transmitter points.

5. RESULTS

5.1 Computation time and memory size

The creation of the system from node and tetrahedra data, including all parts of the asteroid geometry, orbiter points and interpolation of the finite element mesh required approximately 11 GB of memory space and 6 700 seconds (approximately 1 hrs 52 minutes). Out of this, the actual system creation took 652 seconds (approximately 10 minutes) and creating the spatial interpolation matrix accounted for the rest of the computational time.

The minimum computation time of one transmitted signal was 11 400 seconds (approximately 3 hrs 10 minutes). The system size was approximately 4.8 GB. Because the forward simulation was parallelized into 16 processes, the total computation time of the entire simulation, 64 transmitter points, took a minimum of 45 400 seconds (approximately 12 hrs 37 minutes). Not all nodes performed equally well, so a typical expected computation time for the entire forward simulation was approximately 13.5 hours.

5.2 Signal at the antenna

The full-wave computed radar tomography simulation was run to the six different model structures including void space, highly porous deep interior, dielectrically very dense block, and two types of cracks inside the asteroid, in addition to the background model lacking these details. The forward simulation yields data on the signal voltage at the antenna.

The data for each of the model structures is shown in the Figure 5.1. The Figure 5.1(a) shows the received signal at the antenna across the whole computational domain. The first echoes at time interval $[0, 0.1]$ is caused by the spherical outer surface of the domain Ω_2 depicted in the Figure 2.3 and is exactly the same for the background and the detailed model. The first large peak and trough where the signals differ, at time point approximately 0.3, originates from the surface of the asteroid. In the background model (red line), the permittivity of the asteroid interior is constant $\varepsilon_r = 4$ across the whole asteroid interior and hence a more distinct echo is recorded in comparison to each the detailed model (blue line) which includes a surface layer which permittivity is smaller ($\varepsilon_r = 3$). Hence the strength of signal is lower. The time interval approximately $[0.35, 0.5]$ shows signal propagation within the asteroid. The signal at time point approximately 0.5 is from the other side of the asteroid surface layer. Any signal after that comes from the remaining part of the model (surface of Ω_2 and beyond) and is not interesting. The figures from 5.1(b) to 5.1(f) depict the signal at the antenna of each of the models and shows how the

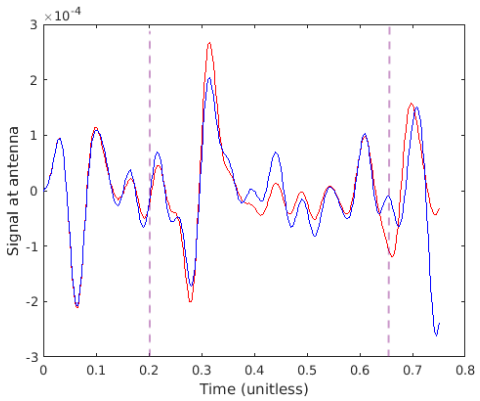

(a) A representative signal across the whole computational domain Ω.

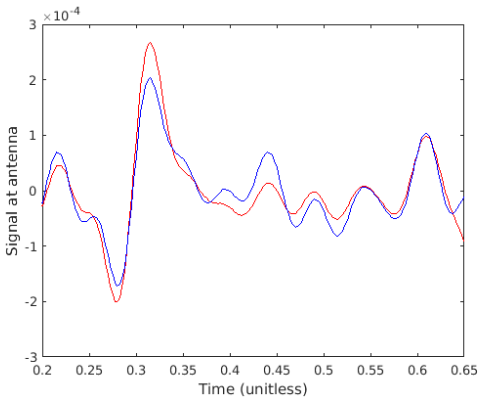

(b) Void in the deep interior.

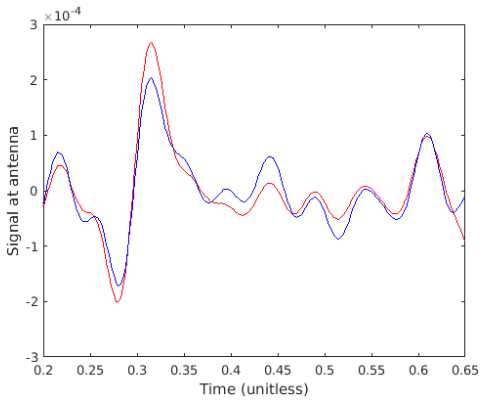

(c) Cavity with highly porous material.

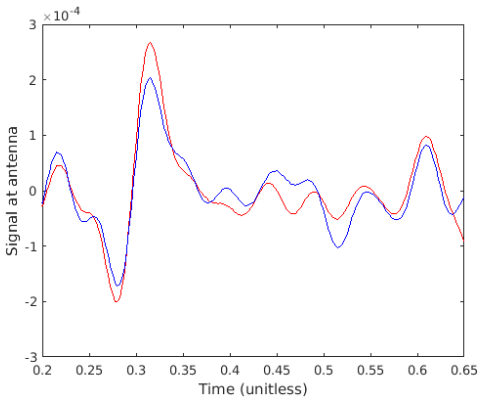

(d) High-permittivity boulder within the deep interior.

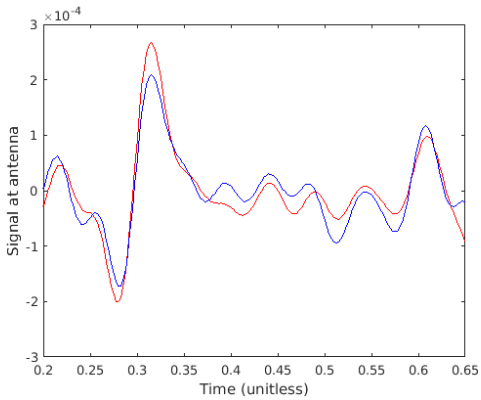

(e) Deep crack.

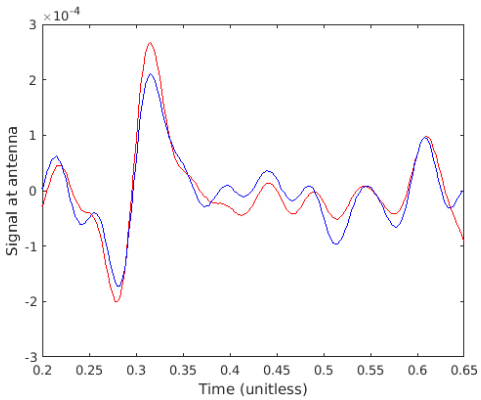

(f) Shallow crack.

Figure 5.1. *Typical antenna signals from a single point source showing how the details of the model (blue) produce different echoes in comparison to the background (red). The background echo is the same in each of the figures. The blue echo originates from the model details. The first detectable differences between the background and the detailed model at approximately* $T = 0.3$ *are in the large peaks which corresponds to the signal echoes at the surface of the asteroid. The echoes originating from structural details can be seen at approximately* $T = 0.4$.

structural details can be detected in the raw signal computed at one transmitter-receiver point. The x-axes of these figures are limited to include only the part of the signal involving the asteroid. The magenta dashed lines in the Figure 5.1(a) indicate the time interval which has been included in the Figures from 5.1(b) to 5.1(f), to emphasize the signal travelling within the asteroid.

The differences in the curves shown in the Figures 5.1(b) to 5.1(f) are due to the differences in how the signal propagates through the asteroid. Especially interesting is to compare the amplitudes of the signals for the void, the cavity with highly porous material, and the dense boulder. The geometrical models of these are identical, but the signal curves show firstly differences in the amplitudes and, in the case of the boulder, also the shape of the received signal. This is to be expected because electromagnetic waves respond to changes in dielectric properties.

When looking at the deep crack and the shallow crack figures (Figures 5.1(e) and 5.1(f), respectively), the differences are minor, but discernible. The shallow crack produces a slightly different echo at time point approximately 0.4. In the deep crack model such detail is not visible, and therefore it is not seen in the signal either.

Each of the model system signals were further analysed by solving the inverse problem to obtain the electrical permittivity values inside the asteroid, and to evaluate the performance of the DISCUS radar with a realistic asteroid geometry and realistic interior structure. The inversion computation was run with regularization parameters of $\alpha = 0.01$ and $\beta = \{0.005, 0.0075\}$ depending on the model. Such parameters produced a workable range of values corresponding to the original model permittivity range. An example of the asteroid permittivity distribution after inversion is shown in the Figure 5.2(c) which demonstrates that the surface layer and the single deep void anomaly can be detected by the radar. It also shows how the simulation produces a radargram similar to the realistic radar measurements (Figure 2.2).

5.3 Void detection

The first investigated interior model is the single, small ellipsoidal void in the body of the asteroid. The exact 3D reference model is shown in the Figure 5.2(a). Looking at the Figures 5.2(b) and 5.2(c) it is evident that such a void space can be recovered by the DISCUS radar simulated in this work. The detection power of the radar is the better in the direction closer to the surface of the asteroid. This is also an expected result, as clear detection of the eastern side of the void would require wave propagation through the asteroid for a long distance. The realistic inhomogeneous structure of the asteroid most likely scatters the waves so that should it reach the interface of the void in the eastern direction, the power of the signal is lost in the background noise.

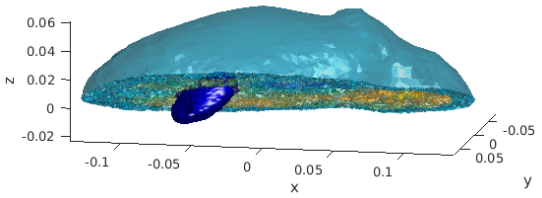

(a) The exact model.

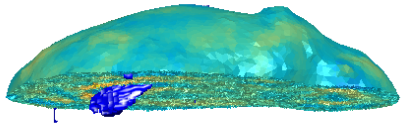

(b) The detected void

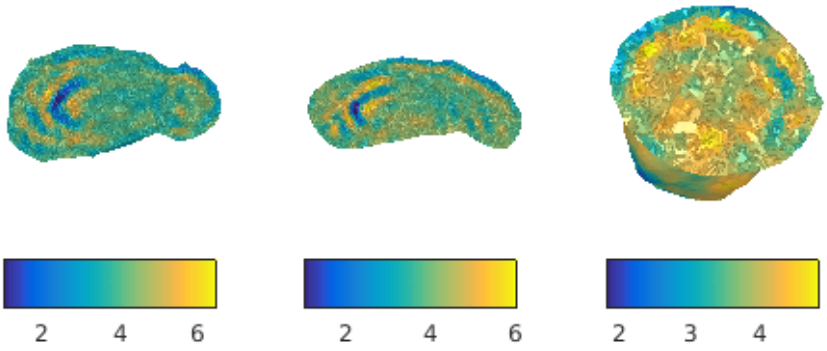

(c) Reconstruction after inversion showing also the surface layer in addition to the detection of the void.

Figure 5.2. *A small deep interior void can be detected by full-wave computed radio tomography. The reconstruction in (c) shows a reconstruction which corresponds to a very realistic radargram. The surface layer and the deep internal void can be detected.*

5.4 Detection of a cavity of highly porous material

The Figure 5.3 shows that the DISCUS radar can also detect highly porous materials with electrical permittivity quite close to that of the surroundings. The Figure 5.3(b) shows that such formation of material can be detected, just like a void space of similar size and position inside the asteroid. The detection of a structure which is less distinct in comparison to the surroundings is not as clear as the detection shown in the case of the void space, but the location of an anomaly is evident in the Figures 5.3(b) and 5.3(c).

5.5 Boulder detection

In this work, the boulder model refers to any electrically high permittivity structure inside the asteroid interior. The structure could be wet concrete type of material or metallic enrichment inside an asteroid. The Figure 5.4 shows that also the high-permittivity structure can be detected. Similar to the low permittivity structures, also here the best detection is obtained of the face closest towards the surface. The deep interior side of the structure remains undetermined.

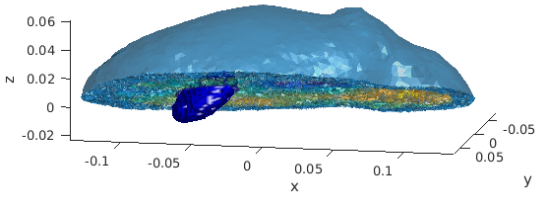

(a) The exact model.

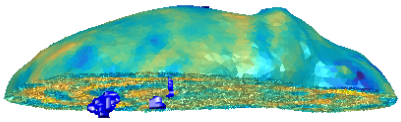

(b) The detected cavity of highly porous material.

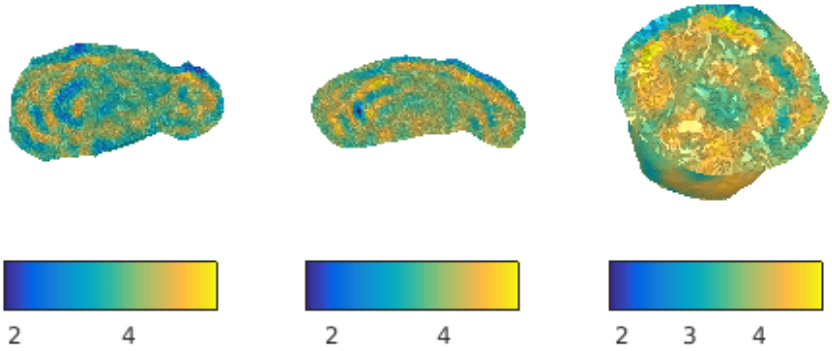

(c) Reconstruction after inversion showing also the surface layer. The highly porous cavity can be seen as enclosed by a higher permittivity layer (yellow).

Figure 5.3. *A cavity of highly porous material can be detected.*

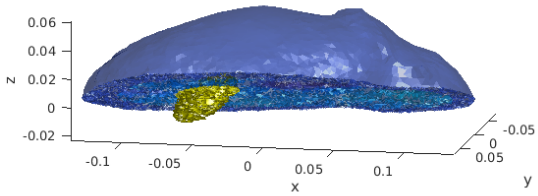

(a) The exact model.

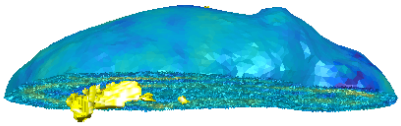

(b) The detected high-permittivity structure, boulder.

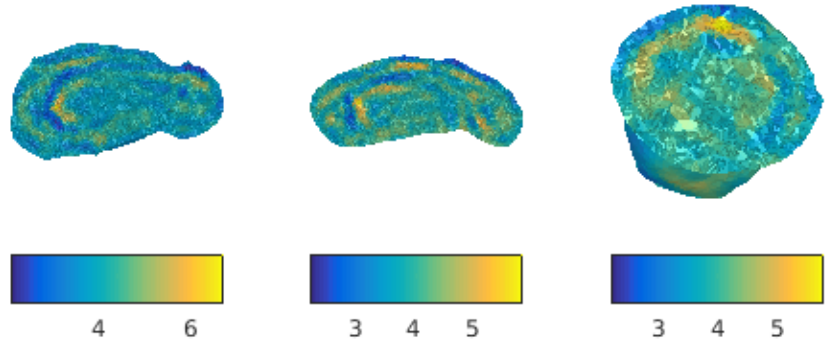

(c) Reconstruction after inversion showing also the surface layer. The high permittivity shape is clearly visible.

Figure 5.4. *A block or boulder of very high relative permittivity value can be detected inside the asteroid.*

5.6 Crack detection

Detection of a crack deep within the asteroid is challenging. The Figure 5.5 shows how an echo is recovered from the deep center of the asteroid, but the shape of the crack and the full extent of it goes uncovered. The Figure 5.5(b) shows how a signal can be obtained from the deep center, but it may be due to the separate arm of the crack shown in the exact model reference (Figure 5.5(a)), and not the crack dissecting the asteroid in the middle.

It is possible that a crack of this size is not large (wide) enough to produce a detectable echo, especially because the crack is deep inside the asteroid and the wave attenuates already before reaching the crack interface. From this simulation it appears to be clear that the crack cannot be detected from the north or the south due to its small diameter. Also, there are apertures around the north and south of the asteroid (Figure 4.2) and therefore a crack oriented like this may not be detected from these directions.

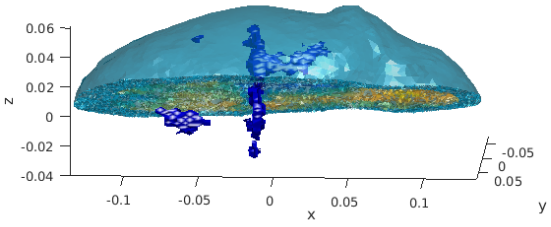

(a) The exact model.

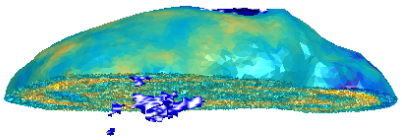

(b) The detected crack in the deep interior

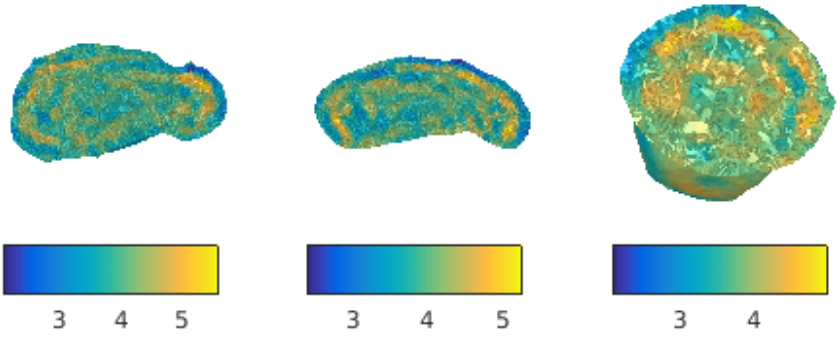

(c) Reconstruction after inversion showing also the surface layer in addition to the detection of the crack.

Figure 5.5. *A deep crack running across the asteroid in north-south direction is hardly detectable by this methodology.*

In the shallow crack model the crack is positioned in the interface of the surface layer and the deep interior. In this case, a clear echo is detected and it is possible to deduce that the anomaly has a complicated shape based on the echo (Figure 5.5(b)). Although the exact shape and especially the tips of the crack cannot be accurately detected, a good approximation of the crack can be obtained. The areas close to the surface of the asteroid are visible and the 3D reconstruction suggests that the echo originates from a shape which

is more complicated than a simple elliptic shape of uniform permittivity. The crack is also visible in the electrical permittivity reconstruction (Figure 5.6(c))

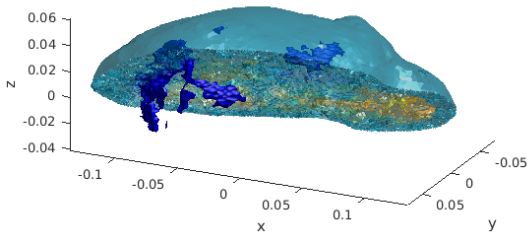

(a) The exact model.

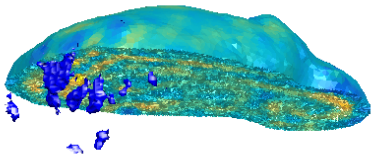

(b) The detected shallow crack.

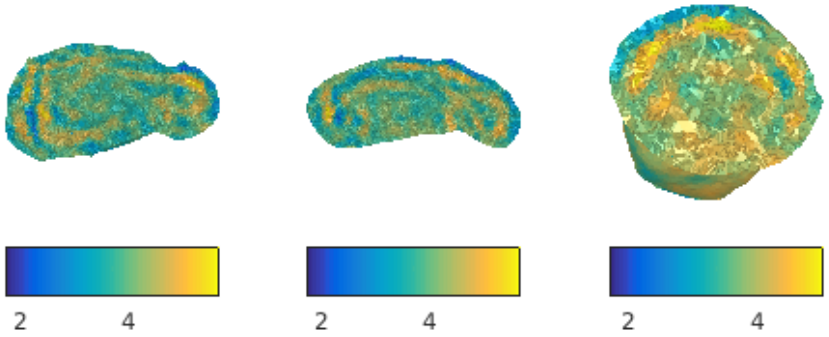

(c) Reconstruction after inversion showing also the surface layer in addition to the detection of the crack.

***Figure 5.6**. A shallow crack with two arms and complicated shape can be detected.*

5.7 Comparison of bistatic to monostatic measurement

The DISCUS radar concept includes a bistatic radar in which one out of the two satellites acts as a transmitter and a receiver, and the other is a receiver only. With such a setup, the measurements can also be carried out as monostatic, i.e. one satellite transmits and receives the signal, and the satellite which acts only as a receiver is ignored. The monostatic radar set-up was investigated by comparing the reconstructions of the deep interior void from the bistatic measurement reported in section 5.3, to the computed monostatic reconstruction (Figure 5.7). The reconstruction of the monostatic measurement is shown is in the Figure 5.7(b)

The results show that both radar set-ups provide clear detection of the void. The bistatic measurement appears to show slightly more prominent shape of the anomaly, but this may not be significant in practical applications. The significance of using a bistatic approach in radar tomography is to provide statistical robustness to the measurements.

(a) Bistatic measurement of deep interior void.

(b) Monostatic measurement of the deep interior void.

Figure 5.7. *Comparison of bistatic and monostatic measurement configuration on the reconstruction of deep interior void. The bistatic set-up provides slightly better reconstruction.*

6. DISCUSSION

The aim of this thesis was to study full-wave radar tomography in a realistic rubble-pile asteroid models and especially to investigate the detection power of simulated deep interior structures in a realistic asteroid. The surface model of the asteroid Itokawa was chosen because it is one of the few asteroids for which there is an abundance of actual real data on its surface and bulk properties [11, 16, 31, 41, 42, 55], and a high-resolution surface model available [5]. The structural models simulated in this thesis were done by combining the data from these sources and extensive investigations [33, 34, 36] to the physical properties of small solar system bodies and how electromagnetic waves behave in such media.

In 2003, Aspaugh et al. proposed a deep interior mission concept to a near-Earth asteroid and conducting radar tomography to detemine the deep interior structures [14]. Since then, the deep interior of a comet 67P/Churyumov-Gerasimenko was studied by a radar in the CONCERT study, a part of European Space Agency's Rosetta mission, and reported that the average permittivity of the comet is approximately 1.26, suggesting a volumetric dust/ice ratio of 0.4 to 2.6 and a porosity of 75 to 85 % [36]. This thesis is a part of the DISCUS concept [15], a proposal to send a bistatic CubeSat to study the deep interior of a rubble-pile asteroid.

To create a realistic deep interior model of the Itokawa model, the dielectric properties of the asteroid were modelled by Gaussian random fields, a well-established method to modelling random spatial structures in geostatistics and earth sciences [25, 26, 38]. They are also used to generate random 3D porous structures [47] and modelling concrete [18] in civil engineering applications.

The deep interior anomalies were added to the Gaussian random field model and the full-wave computed radar tomography simulation was run on five different systems to determine the detection power of the DISCUS radar. Special interest was taken to model macroporosity with void cavity and a cavity with highly porous material, as evidence from the Hayabusa mission suggests that the macroporosity of asteroid Itokawa is up to 41 percent [31]. Confirming these measurements with direct radar observations would be very interesting. The full-wave simulation results in this work show that macropores can be detected by radar tomography.

The results in this thesis show that the deep interior anomaly detection is the best in the direction where the most area of the anomaly is. The largest faces of the anomalous ellipsoidal voids and cavities towards the surface of the asteroid are clearly detectable, as is the shallow crack at the interface of the deep interior and the surface layer of the

asteroid. A crack in the deep interior cannot be detected as clearly, although a mild echo suggesting an anomaly can be reconstructed. The exact shapes of the cracks, or especially the tips of the cracks cannot be accurately reconstructed, neither the narrow heads of the ellipsoids or the faces of the ellipsoids which are towards the deep interior of the asteroid. These are explained by the fact that electromagnetic waves attenuate and scatter as they travel within the asteroid and therefore echoes from such parts are not easily detectable and signals may be obstructed by noise.

The results show that the exact permittivity distribution of the complete asteroid model, especially of the deep interior, cannot be reconstructed, but that the anomalies can be detected and their relative permittivities estimated. The higher the difference between the Gaussian random field background and the anomaly, the better the detection was. The clearly defined ellipsoidal anomalies were detected the best, however, the results for the simulated shallow crack showed very clearly that it is possible to detect even complicated void structures near the surface of the asteroid. The quality of reconstruction and exact permittivity values were dependent on the the regularization parameters of the inversion. It was also shown that the inverse reconstructions of the models exhibited similar wavefront properties as radargrams of actual radar measurement data.

The DISCUS concept includes a bistatic radar configuration in which one of the satellites acts as a transmitter and receiver and the other as a receiver only. Using two satellite configuration provides statistical robustness to the measurements, but sufficient and clear detection of interior structures can be carried out with a monostatic, a single-satellite, radar system as well, as was shown in the results. The detection of the deep interior void was clear with monostatic and bistatic measurements, the bistatic one being slightly more pronounced.

The earlier publications [46, 52] on this methodology included 2D and 3D models of simpler structures than the asteroid model developed in this thesis. The earlier work, in which the interior permittivity of the asteroid was constant and the investigated asteroid geometries were smoother and more spherical in shape, provided very clear reconstructions of deep interior voids. The results presented in this thesis show that in a realistic case the detection will not be as exact and that the detection is dependent on the dielectric properties of the asteroid body and the geometry of the asteroid, as the structures closer to the surface are detected more clearly than those which require the waves to travel long distances inside the asteroid.

The computational framework developed in this thesis includes a simple pipeline for simulating realistic asteroid interiors based on a finite element mesh structural model. It was also shown in this thesis that full-wave (full-bandwidth) data can be computed and inverted for the realistic rubble-pile asteroid using a high-end computing cluster equipped with state-of-the-art GPUs, in a reasonable time within one day by parallelizing the computation.

Further development of the computational model in the future is to extend the analysis of the received signal to the envelope of the received wave. The analysis in this work involved only the reception of the the modulated signal across the whole bandwidth. By combining the data from the modulated signal and the envelope, the accuracy of the method can be further improved.

Other future work on this topic is to extend the simulation methodology to include a satellite fly-by model in which the measurement points are not from an orbiter but rather a satellite passing by an asteroid at a distance. This would be advantageous in deep space missions where satellites could map the deep interior of the bodies they pass by while travelling to the target solar system body.

The source code used in this thesis will be later prepared for publication and distribution as an open-source pipeline for radar tomography simulations. The same approach can also be used in other fields, for example biomedical applications, where tomography is used to map the deep interior of bodies.

BIBLIOGRAPHY

[1] About nvidia - ai computing. https://www.nvidia.com/en-us/about-nvidia/ai-computing/. Accessed 17 May 2018.

[2] Discovery statistics. https://cneos.jpl.nasa.gov/stats/totals.html. Center for Near Earth Object Studies, NASA, accessed 13 July 2018.

[3] Evidence detected of lake beneath the surface of mars. https://edition.cnn.com/2018/07/25/world/mars-subsurface-water-lake-evidence/index.html. Accessed 25 July 2018.

[4] Gpu programming in matlab. https://se.mathworks.com/company/newsletters/articles/gpu-programming-in-matlab.html. Accessed 17 May 2018.

[5] Hayabusa project science data archive, itokawa shape model. https://darts.isas.jaxa.jp/planet/project/hayabusa/shape.pl. Accessed 18 December, 2017.

[6] Japan aerospace exploration agency, hayabusa project. http://global.jaxa.jp/projects/sat/muses_c/index.html. Accessed 18 January 2018.

[7] Liquid water 'lake' revealed on mars. https://www.bbc.co.uk/news/science-environment-44952710. Accessed 25 July 2018.

[8] Marsista löytyi jäätikön alta suolavesijärvi - suomalaisasiantuntija pitää uutista merkittävänä. https://yle.fi/uutiset/3-10322790. Accessed 25 July 2018.

[9] New study reveals twice as many asteroids as previously believed. http://www.spaceref.com/news/viewpr.html?pid=7925. Accessed 13 July 2018.

[10] Underground lake found on mars, raising possibility of life. https://www.reuters.com/article/us-space-mars/underground-lake-found-on-mars-raising-possibility-of-life-idUSKBN1KF1Z8. Accessed 25 July 2018.

[11] M. Abe, Y. Takagi, K. Kitazato, S. Abe, T. Hiroi, F. Vilas, B. E. Clark, P. A. Abell, S. M. Lederer, K. S. Jarvis, T. Nimura, Y. Ueda, and A. Fujiwara. Near-infrared spectral results of asteroid itokawa from the hayabusa spacecraft. *Science*, 312(5778):1334–1338, 2006.

[12] P. Abrahamsen. *A review of Gaussian random fields and correlation functions*. Norwegian Computing Center, Oslo, Norway, 2nd edition, 1997.

[13] A. Annan. Electromagnetic principles of ground penetrating radar. In H. M. Jol, editor, *Ground Penetrating Radar Theory and Applications*, chapter 1. Elsevier Science, 2008.

[14] E. Asphaug, M. J. S. Belton, A. Cangahuala, L. Keith, K. Klaasen, L. McFadden, G. Neumann, S. J. Ostro, R. Reinert, A. Safaeinili, D. J. Scheeres, and D. K. Yeomans. Exploring Asteroid Interiors: The Deep Interior Mission Concept. In S. Mackwell and E. Stansbery, editors, *Lunar and Planetary Science Conference*, volume 34 of *Lunar and Planetary Inst. Technical Report*, Mar. 2003.

[15] P. Bambach, J. Deller, E. Vilenius, S. Pursiainen, M. Takala, H. M. Braun, H. Lentz, and M. Wittig. DISCUS - The Deep Interior Scanning CubeSat mission to a rubble pile near-Earth asteroid. *ArXiv e-prints*, May 2018.

[16] O. S. Barnouin-Jha, A. F. Cheng, T. Mukai, S. Abe, N. Hirata, R. Nakamura, R. W. Gaskell, J. Saito, and B. E. Clark. Small-scale topography of 25143 itokawa from the hayabusa laser altimeter. *Icarus*, 198(1):108 – 124, 2008.

[17] K. Berry, B. Sutter, A. May, K. Williams, B. Barbee, M. Beckman, and B. Williams. Osiris-rex touch-and-go (tag) mission design and analysis. 149:667–678, 01 2013.

[18] Bićanić, R. Nenad, de Borst, H. mang, and M. Gunther, editors. *Computational modelling of concrete structures*, EURO-C, Leiden, The Netherlands, 7 2010. The organization, CRC Press/Balkema, Taylor & Francis Group. ISBN: 978-0-415-58479-1.

[19] H. Braun, H. Lentz, and A. Woode. A planetary into-the-ground radar and altimeter (pira). Technical report, The institution that published, 11 1997.

[20] S. J. Bus and R. P. Binzel. Phase II of the Small Main-Belt Asteroid Spectroscopic Survey. A Feature-Based Taxonomy. *Icarus*, 158:146–177, July 2002.

[21] N. J. Cassidy. Electrical and magnetic properties of rocks solids and fluids. In H. M. Jol, editor, *Ground Penetrating Radar Theory and Applications*, chapter 2. Elsevier Science, 2008.

[22] I. Catapano, L. Crocco, Y. Krellmann, G. Triltzsch, and F. Soldovieri. A tomographic approach for helicopter-borne ground penetrating radar imaging. *IEEE Geoscience and Remote Sensing Letters*, 9(3):378–382, May 2012.

[23] I. Catapano, L. Crocco, F. Soldovieri, R. Lanari, C. Facchinetti, F. Longo, R. Formaro, G. Alberti, D. Adirosi, and R. Persico. Airborne gpr surveys via tomographic imaging: An analysis of the reconstruction capabilities. In *2012 14th International Conference on Ground Penetrating Radar (GPR)*, pages 310–314, June 2012.

[24] C. R. Chapman, D. Morrison, and B. Zellner. Surface properties of asteroids: A synthesis of polarimetry, radiometry, and spectrophotometry. *Icarus*, 25(1):104 – 130, 1975.

[25] J.-P. Chilès and D. P. *Geostatistics: Modeling Spatial Uncertainty*. John Wiley & Sons, Inc., Hoboken, New Jersey, USA, 2 edition, 2012.

[26] G. Christakos. *Random field models in earth sciences*. Dover Publications, Inc., Mineola, New York, USA, 2005.

[27] P. Cignoni, M. Callieri, M. Corsini, M. Dellepiane, F. Ganovelli, and G. Ranzuglia. MeshLab: an Open-Source Mesh Processing Tool. In V. Scarano, R. D. Chiara, and U. Erra, editors, *Eurographics Italian Chapter Conference*. The Eurographics Association, 2008.

[28] P. Constantine. Random field simulation, 2012. Version 1.5 retrieved March 23, 2018.

[29] L. C. Evans. *Partial Differential Equations (Graduate Studies in Mathematics)*. American Mathematical Society, Providence, RI, 1998.

[30] L. Fu, S. Liu, L. Liu, and L. Lei. Development of an airborne ground penetrating radar system: Antenna design, laboratory experiment, and numerical simulation. *IEEE Journal of Selected Topics in Applied Earth Observations and Remote Sensing*, 7(3):761–766, March 2014.

[31] A. Fujiwara, J. Kawaguchi, D. K. Yeomans, M. Abe, T. Mukai, T. Okada, J. Saito, H. Yano, M. Yoshikawa, D. J. Scheeres, O. Barnouin-Jha, A. F. Cheng, H. Demura, R. W. Gaskell, N. Hirata, H. Ikeda, T. Kominato, H. Miyamoto, A. M. Nakamura, R. Nakamura, S. Sasaki, and K. Uesugi. The rubble-pile asteroid itokawa as observed by hayabusa. *Science*, 312(5778):1330–1334, 2006.

[32] C. Geuzaine and J.-F. Remacle. Gmsh: A 3-d finite element mesh generator with built-in pre- and post-processing facilities. *International Journal for Numerical Methods in Engineering*, 79(11):1309–1331, 2009.

[33] A. Herique, B. Agnus, E. Asphaug, A. Barucci, P. Beck, J. Bellerose, J. Biele, L. Bonal, P. Bousquet, L. Bruzzone, C. Buck, I. Carnelli, A. Cheng, V. Ciarletti, M. Delbo, J. Du, X. Du, C. Eyraud, W. Fa, J. G. Fernandez, O. Gassot, R. Granados-Alfaro, S. Green, B. Grieger, J. Grundmann, J. Grygorczuk, R. Hahnel, E. Heggy, T.-M. Ho, O. Karatekin, Y. Kasaba, T. Kobayashi, W. Kofman, C. Krause, A. Kumamoto, M. Kuppers, M. Laabs, C. Lange, J. Lasue, A. Levasseur-Regourd, A. Mallet, P. Michel, S. Mottola, N. Murdoch, M. Mutze, J. Oberst, R. Orosei, D. Plettemeier, S. Rochat, R. RodriguezSuquet, Y. Rogez, P. Schaffer, C. Snodgrass, J.-C. Souyris, M. Tokarz, S. Ulamec, J.-E. Wahlund,

and S. Zine. Direct observations of asteroid interior and regolith structure: Science measurement requirements. *Advances in Space Research*, 2017.

[34] W. Kofman. Radar techniques to study subsurfaces and interiors of the solar system objects. In *2012 19th International Conference on Microwaves, Radar Wireless Communications*, volume 2, pages 409–412, May 2012.

[35] W. Kofman, Y. Barbin, J. Klinger, A.-C. Levasseur-Regourd, J.-P. Barriot, A. Herique, T. Hagfors, E. Nielsen, E. GrÃŒn, P. Edenhofer, H. Kochan, G. Picardi, R. Seu, J. van Zyl, C. Elachi, J. Melosh, J. Veverka, P. Weissman, L. Svedhem, S. Hamran, and I. Williams. Comet nucleus sounding experiment by radiowave transmission. *Advances in Space Research*, 21(11):1589 – 1598, 1998.

[36] W. Kofman, A. Herique, Y. Barbin, J.-P. Barriot, V. Ciarletti, S. Clifford, P. Edenhofer, C. Elachi, C. Eyraud, J.-P. Goutail, E. Heggy, L. Jorda, J. Lasue, A.-C. Levasseur-Regourd, E. Nielsen, P. Pasquero, F. Preusker, P. Puget, D. Plettemeier, Y. Rogez, H. Sierks, C. Statz, H. Svedhem, I. Williams, S. Zine, and J. Van Zyl. Properties of the 67p/churyumov-gerasimenko interior revealed by consert radar. *Science*, 349(6247), 2015.

[37] W. Kofman, A. Herique, J.-P. Goutail, T. Hagfors, I. P. Williams, E. Nielsen, J.-P. Barriot, Y. Barbin, C. Elachi, P. Edenhofer, A.-C. Levasseur-Regourd, D. Plettemeier, G. Picardi, and V. Seu, R.and Svedhem. The comet nucleus sounding experiment by radiowave transmission (consert): A short description of the instrument and of the commissioning stages. *Space Science Reviews*, 128(1):413–432, Feb 2007.

[38] C. Lantuéjoul. *Geostatistical Simulation, Models and algorithms*. Springer-Verlag GmbH, Heidelberg, Germany, 2002.

[39] S. Lowry, P. Weissman, S. Duddy, B. Rozitis, A. Fitzsimmons, S. Green, M. Hicks, C. Snodgrass, S. Wolters, S. Chesley, J. Pittichová, and P. V. Oers. The internal structure of asteroid (25143) itokawa as revealed by detection of yorp spin-up. *Astronomy and Astrophysics*, 562:(A48) 1–9, February 2014.

[40] P. Michel, A. Cheng, M. Kuppers, P. Pravec, J. Blum, M. Delbo, S. Green, P. Rosenblatt, K. Tsiganis, J. Vincent, J. Biele, V. Ciarletti, A. Herique, S. Ulamec, I. Carnelli, A. Galvez, L. Benner, S. Naidu, O. Barnouin, D. Richardson, A. Rivkin, P. Scheirich, N. Moskovitz, A. Thirouin, S. Schwartz, A. C. Bagatin, and Y. Yu. Science case for the asteroid impact mission (aim): A component of the asteroid impact & deflection assessment (aida) mission. *Advances in Space Research*, 57(12):2529 – 2547, 2016.

[41] T. Nakamura, T. Noguchi, M. Tanaka, M. E. Zolensky, M. Kimura, A. Tsuchiyama, A. Nakato, T. Ogami, H. Ishida, M. Uesugi, T. Yada, K. Shirai, A. Fujimura, R. Okazaki, S. A. Sandford, Y. Ishibashi, M. Abe, T. Okada,

M. Ueno, T. Mukai, M. Yoshikawa, and J. Kawaguchi. Itokawa dust particles: A direct link between s-type asteroids and ordinary chondrites. *Science*, 333(6046):1113–1116, 2011.

[42] T. Okada, K. Shirai, Y. Yamamoto, T. Arai, K. Ogawa, K. Hosono, and M. Kato. X-ray fluorescence spectrometry of asteroid itokawa by hayabusa. *Science*, 312(5778):1338–1341, 2006.

[43] R. Orosei, S. E. Lauro, E. Pettinelli, A. Cicchetti, M. Coradini, B. Cosciotti, F. Di Paolo, E. Flamini, E. Mattei, M. Pajola, F. Soldovieri, M. Cartacci, F. Cassenti, A. Frigeri, S. Giuppi, R. Martufi, A. Masdea, G. Mitri, C. Nenna, R. Noschese, M. Restano, and R. Seu. Radar evidence of subglacial liquid water on mars. *Science*, 2018.

[44] L. J. Porcello, R. L. Jordan, J. S. Zelenka, G. F. Adams, R. J. Phillips, W. E. Brown, S. H. Ward, and P. L. Jackson. The apollo lunar sounder radar system. *Proceedings of the IEEE*, 62(6):769–783, June 1974.

[45] P. Pravec and A. W. Harris. Fast and slow rotation of asteroids. *Icarus*, 148(1):12 – 20, 2000.

[46] S. Pursiainen and M. Kaasalainen. Orbiter-to-orbiter tomography: A potential approach for small solar system bodies. *IEEE Transactions on Aerospace and Electronic Systems*, 52(6):2747–2759, 2016.

[47] A. P. Roberts and E. J. Garboczi. Computation of the linear elastic properties of random porous materials with a wide variety of microstructure. *Proceedings of the Royal Society of London A: Mathematical, Physical and Engineering Sciences*, 458(2021):1033–1054, 2002.

[48] D. S. Lauretta, S. S. Balram-Knutson, E. Beshore, W. Boynton, C. Drouet dAubigny, D. N. DellaGiustina, H. L. Enos, D. R. Gholish, C. Hergenrother, E. S. Howell, C. A. Johnson, E. T. Morton, M. C. Nolan, B. Rizk, H. L. Roper, A. E. Bartels, B. Bos, J. Dworkin, D. E. Highsmith, and S. A. Sandford. Osiris-rex: Sample return from asteroid (101955) bennu. 02 2017.

[49] J. Saito, H. Miyamoto, R. Nakamura, M. Ishiguro, T. Michikami, A. M. Nakamura, H. Demura, S. Sasaki, N. Hirata, C. Honda, A. Yamamoto, Y. Yokota, T. Fuse, F. Yoshida, D. J. Tholen, R. W. Gaskell, T. Hashimoto, T. Kubota, Y. Higuchi, T. Nakamura, P. Smith, K. Hiraoka, T. Honda, S. Kobayashi, M. Furuya, N. Matsumoto, E. Nemoto, A. Yukishita, K. Kitazato, B. Dermawan, A. Sogame, J. Terazono, C. Shinohara, and H. Akiyama. Detailed images of asteroid 25143 itokawa from hayabusa. *Science*, 312(5778):1341–1344, 2006.

[50] D. Scheeres and R. Gaskell. Effect of density inhomogeneity on yorp: The case of itokawa. 198:125–129, 05 2008.

[51] F. Soldovieri, I. Catapano, and G. Ludeno. Microwave tomography for an effective imaging in GPR on UAV/airborne observational platforms. In *EGU General Assembly Conference Abstracts*, volume 19 of *EGU General Assembly Conference Abstracts*, page 12415, Apr. 2017.

[52] M. Takala, P. Bambach, J. Deller, E. Vilenius, M. Witting, H. Lentz, H. Braun, M. Kaasalainen, and S. Pursiainen. Far-field inversion for the deep interior scanning cubesat. *submitted to an IEEE joural*, in press.

[53] D. J. Tholen. Asteroid taxonomic classifications. In R. P. Binzel, T. Gehrels, and M. S. Matthews, editors, *Asteroids II*, pages 1139–1150, 1989.

[54] L.-I. Tolonen. Realistisen asteroidimallin kolmiulotteisen elementtiverkon generointi. Bachelor's thesis, Tampere University of Technology, 2018.

[55] A. Tsuchiyama, M. Uesugi, T. Matsushima, T. Michikami, T. Kadono, T. Nakamura, K. Uesugi, T. Nakano, S. A. Sandford, R. Noguchi, T. Matsumoto, J. Matsuno, T. Nagano, Y. Imai, A. Takeuchi, Y. Suzuki, T. Ogami, J. Katagiri, M. Ebihara, T. R. Ireland, F. Kitajima, K. Nagao, H. Naraoka, T. Noguchi, R. Okazaki, H. Yurimoto, M. E. Zolensky, T. Mukai, M. Abe, T. Yada, A. Fujimura, M. Yoshikawa, and J. Kawaguchi. Three-dimensional structure of hayabusa samples: Origin and evolution of itokawa regolith. *Science*, 333(6046):1125–1128, 2011.

[56] Y. Tsuda, M. Yoshikawa, M. Abe, H. Minamino, and S. Nakazawa. System design of the hayabusa 2 – asteroid sample return mission to 1999 ju3. *Acta Astronautica*, 91:356 – 362, 2013.